Supplementary Information

Guided Assembly of Well-Defined Hierarchical Nanoporous Polymers by Lewis Acid–Base Interactions

Wenliang Song, Yu Zhang, Anuraj Varyambath, Il Kim[*]

BK21 PLUS Centre for Advanced Chemical Technology, Department of Polymer Science and Engineering, Pusan National University, Pusan 609-735, Republic of Korea.
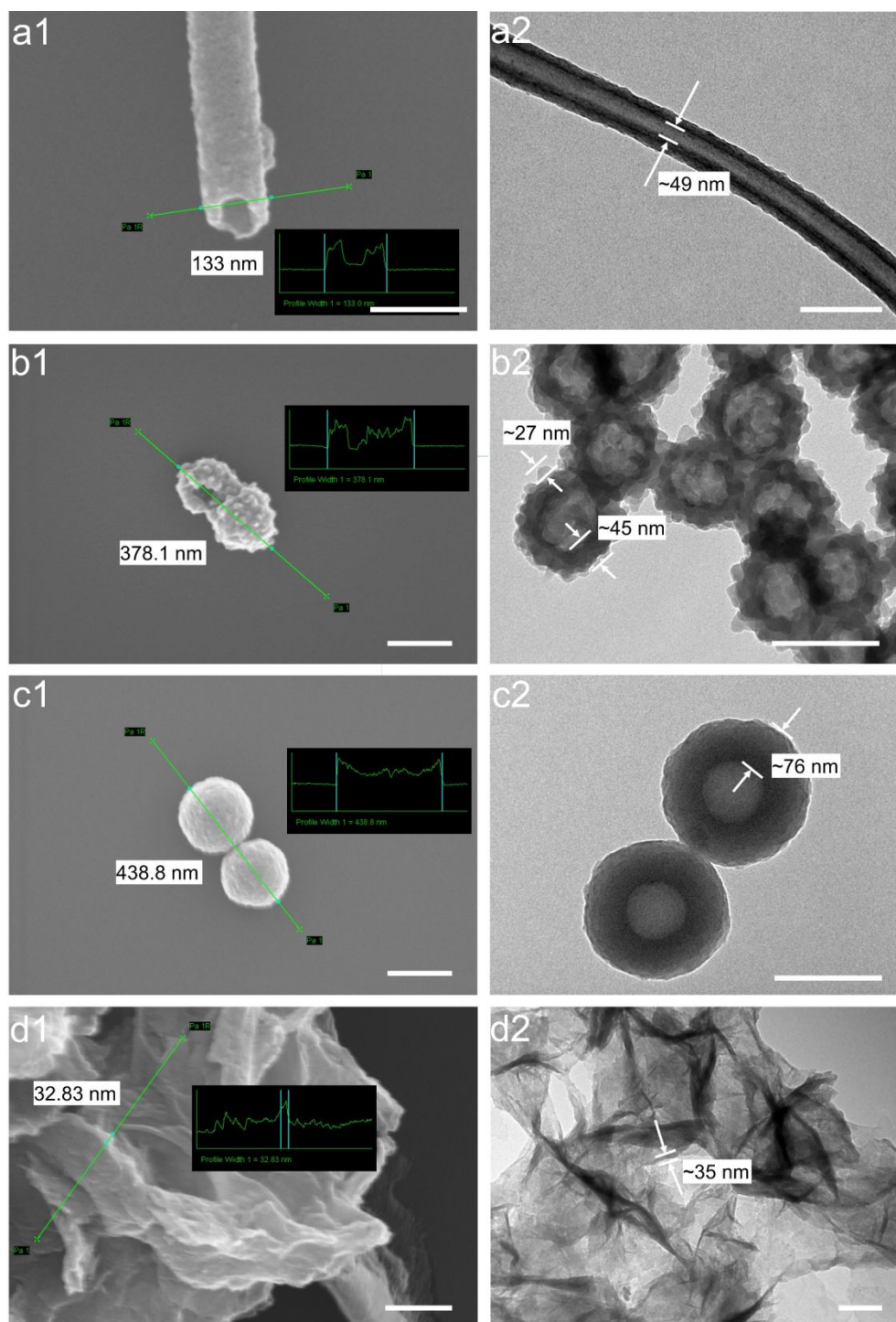
This file includes

Figures S1-53

Table S1-10

Reference S1-18

Figures

Figure S1. Characterizations of the HCP assemblies. Vector profiles of the (a1) HNTs, (b1) HHNP-B, (c1) HHNP-N and (d1) HNSs, respectively. Insets of (a1), (b1), (c1), (d1) show the surface topologies and the diameters of the corresponding subjects (the distance of the blue line) from HNTs, HHNP-B, HHNP-N and HNSs, respectively. TEM images of the (a2) HNTs, (b2) HHNP-B, (c2) HHNP-N and (d2) HNSs, respectively. Scale bars: 200 nm.
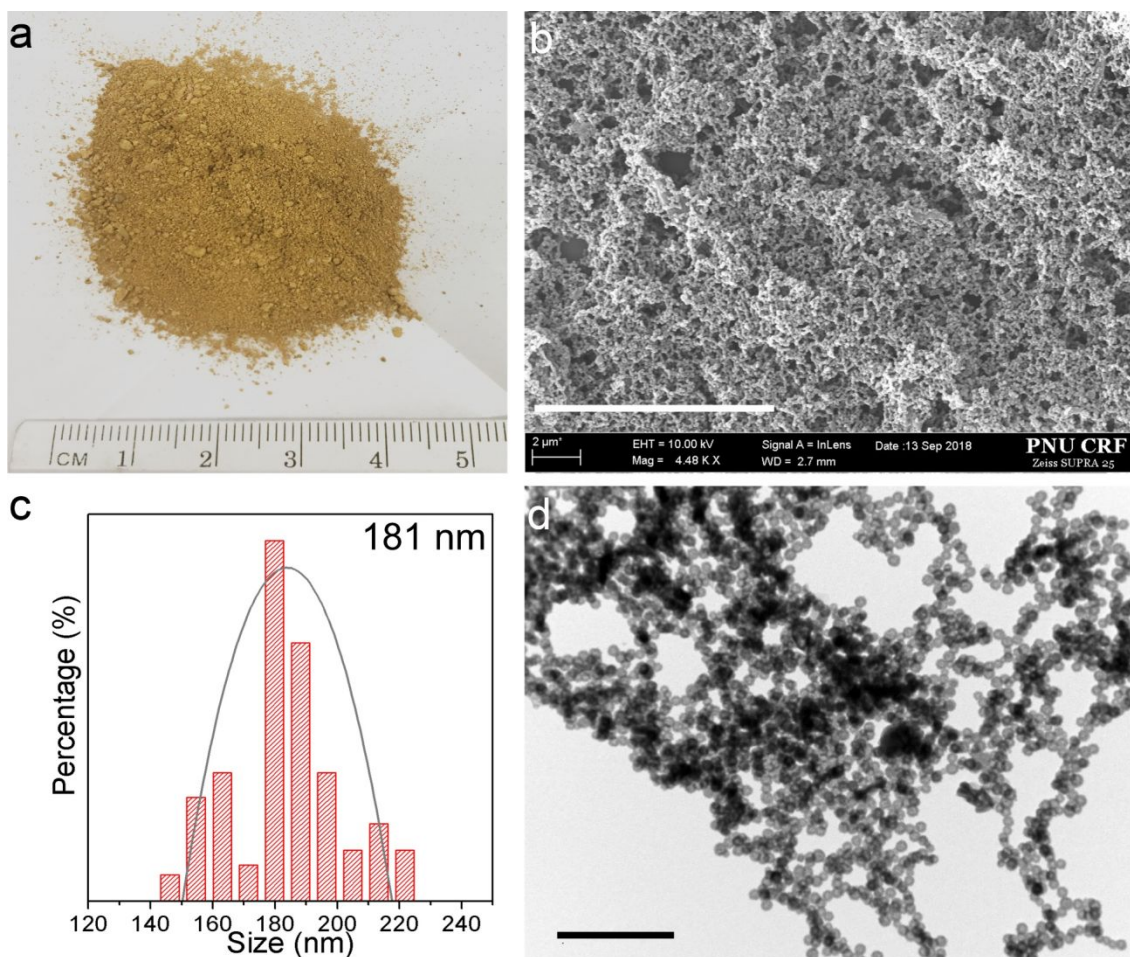
Figure S2. Detail information of the HHNP-B assemblies. (a) Optical photograph, (b) SEM image, (c) size distribution, and (d) TEM image of the HHNP-B, indicating the mass production of hollow polymer nanospheres with high yield. Scale bars: 10 μm in b and 2 μm in d.
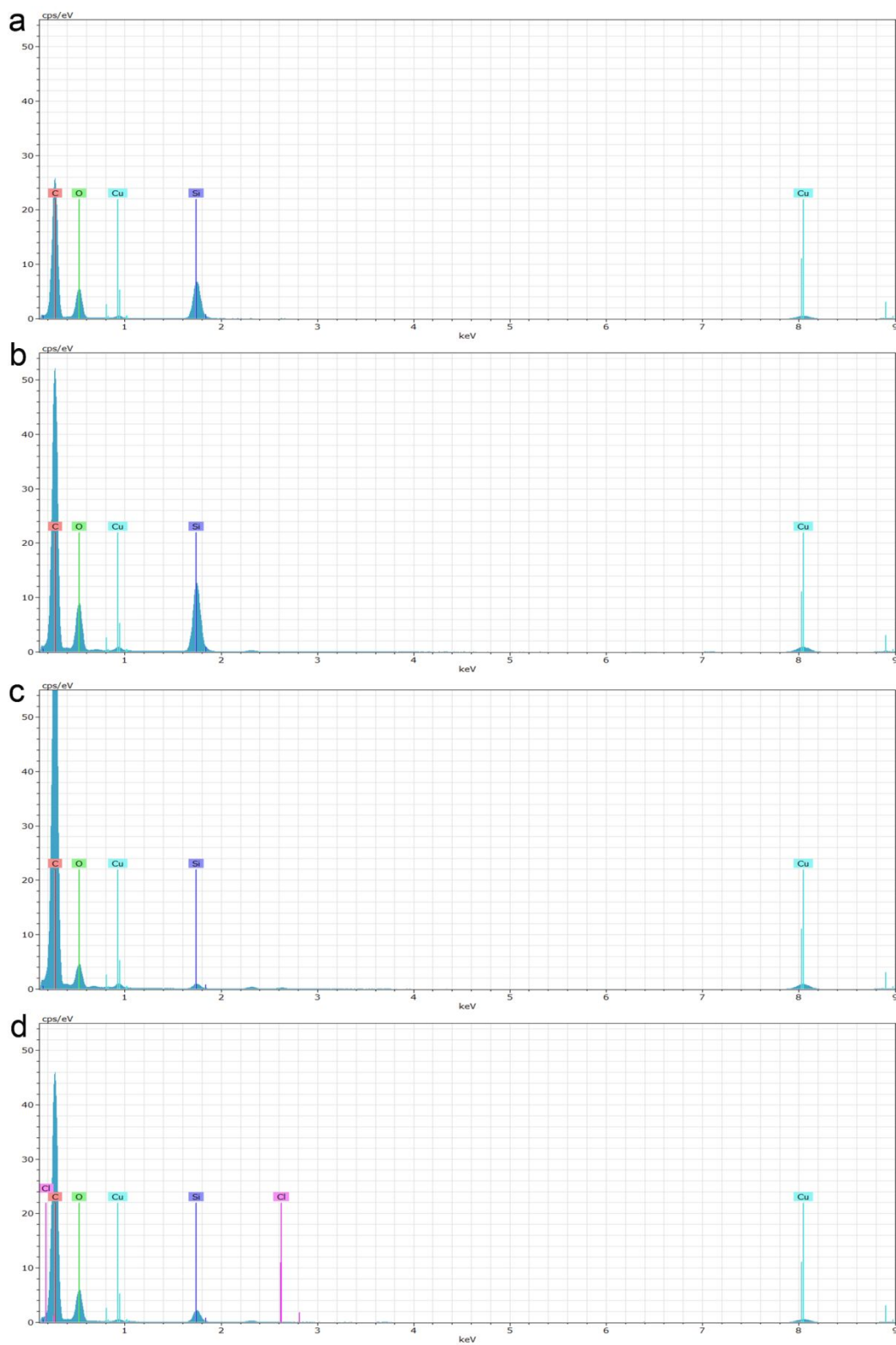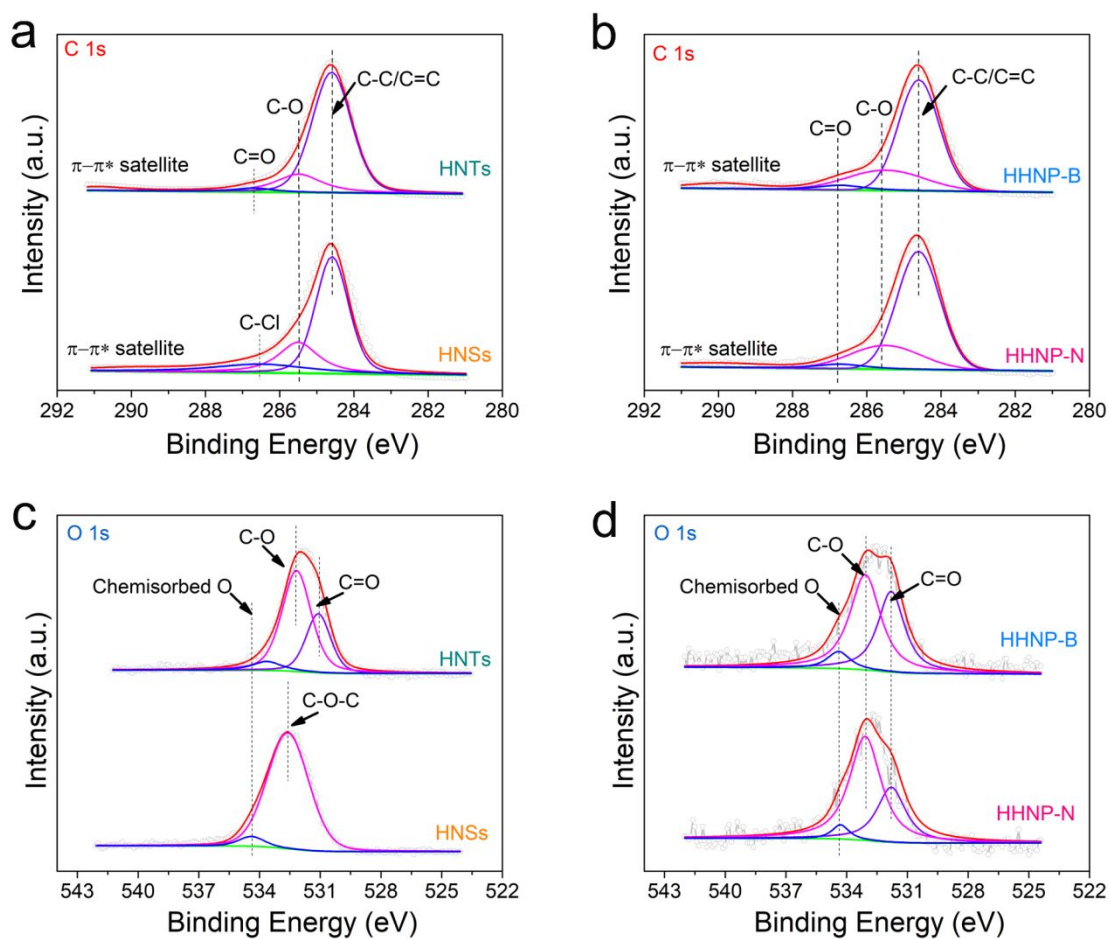
Figure S3. Energy-dispersive X-ray spectroscopy (EDX) spectra for HCPs. (a) HNTs, (b) HHNP-B, (c) HHNP-N, and (d) HNSs, the peaks related on the C, O, Cl, Si, Cu, where the Cu peaks are from the mesh of the TEM grids and the Si peak is from the background.
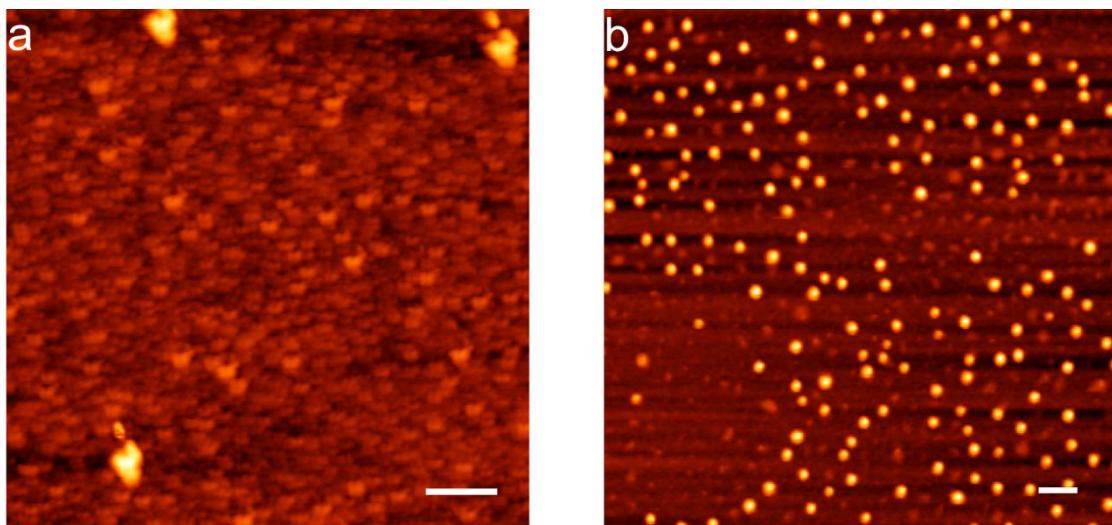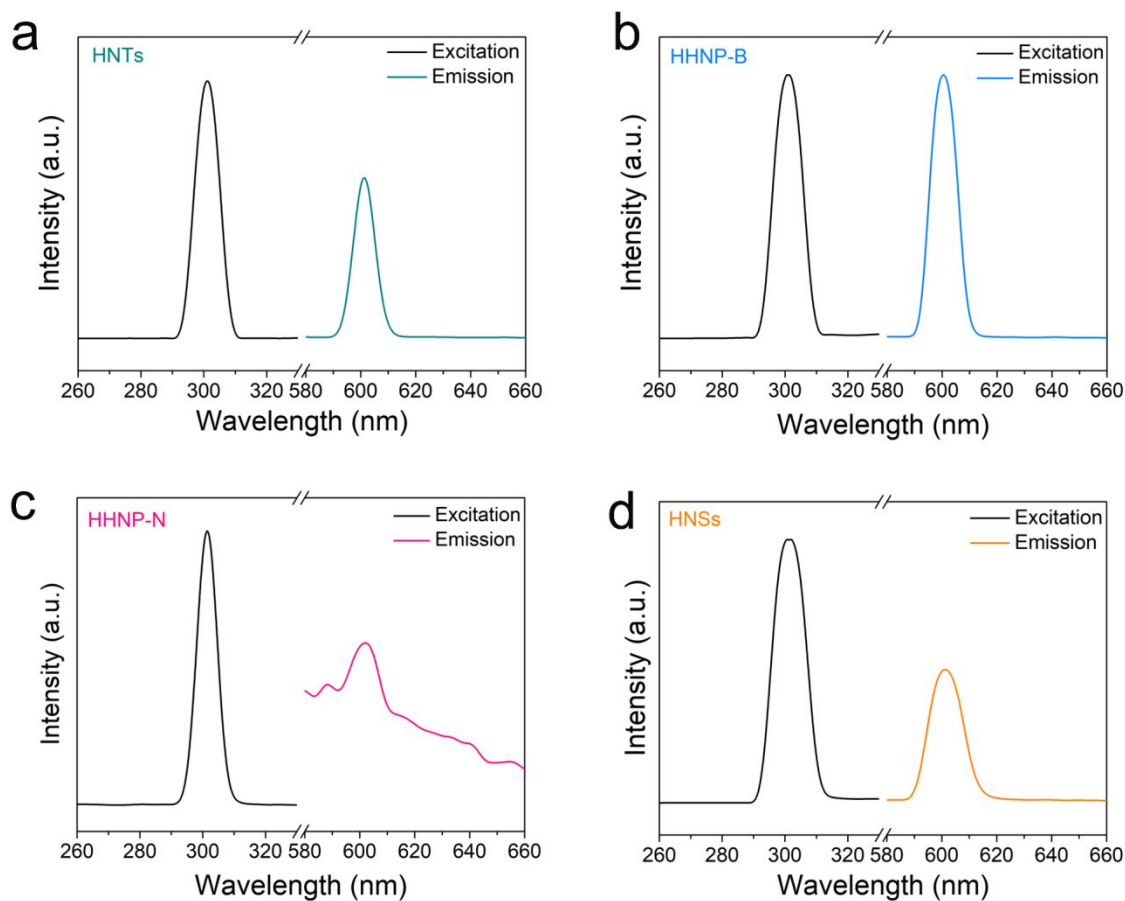
Figure S4. AFM images of HHNPs. (a) HHNP-B, and (b) HHNP-N. Scale bars: 500 nm.

Figure S5. XPS spectra of HCPs. Deconvoluted XPS spectra for (a, b) C 1s and (c, d) O 1s. The formation of ether linkage (C–O–CH$_3$) in the HNSs, which was suspected to be formed during washing HNSs with methanol and the unreacted chlorines being replaced by methoxy groups.

5

Figure S6. Fluorescence characterization of morphology-controlled HCPs. The fluorescence spectra of (a) HNTs, (b) HHNP-B, (c) HHNP-N, and (d) HNSs, the excitation is 300 nm, and the emission peak is around 600 nm.
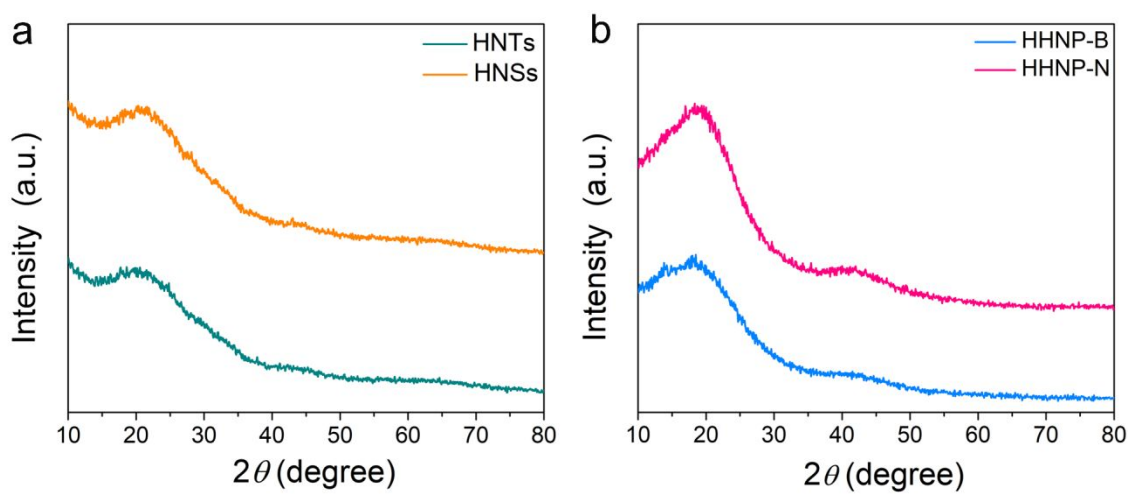
Figure S7. Powder XRD profiles for morphology-controlled HCPs.
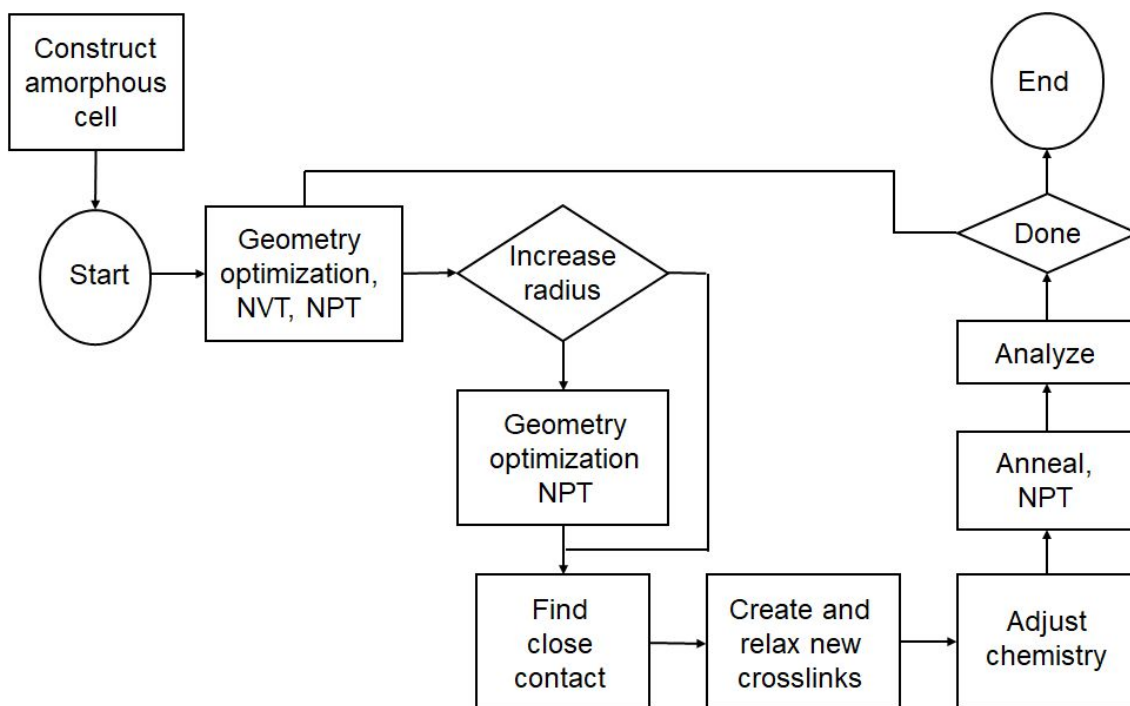
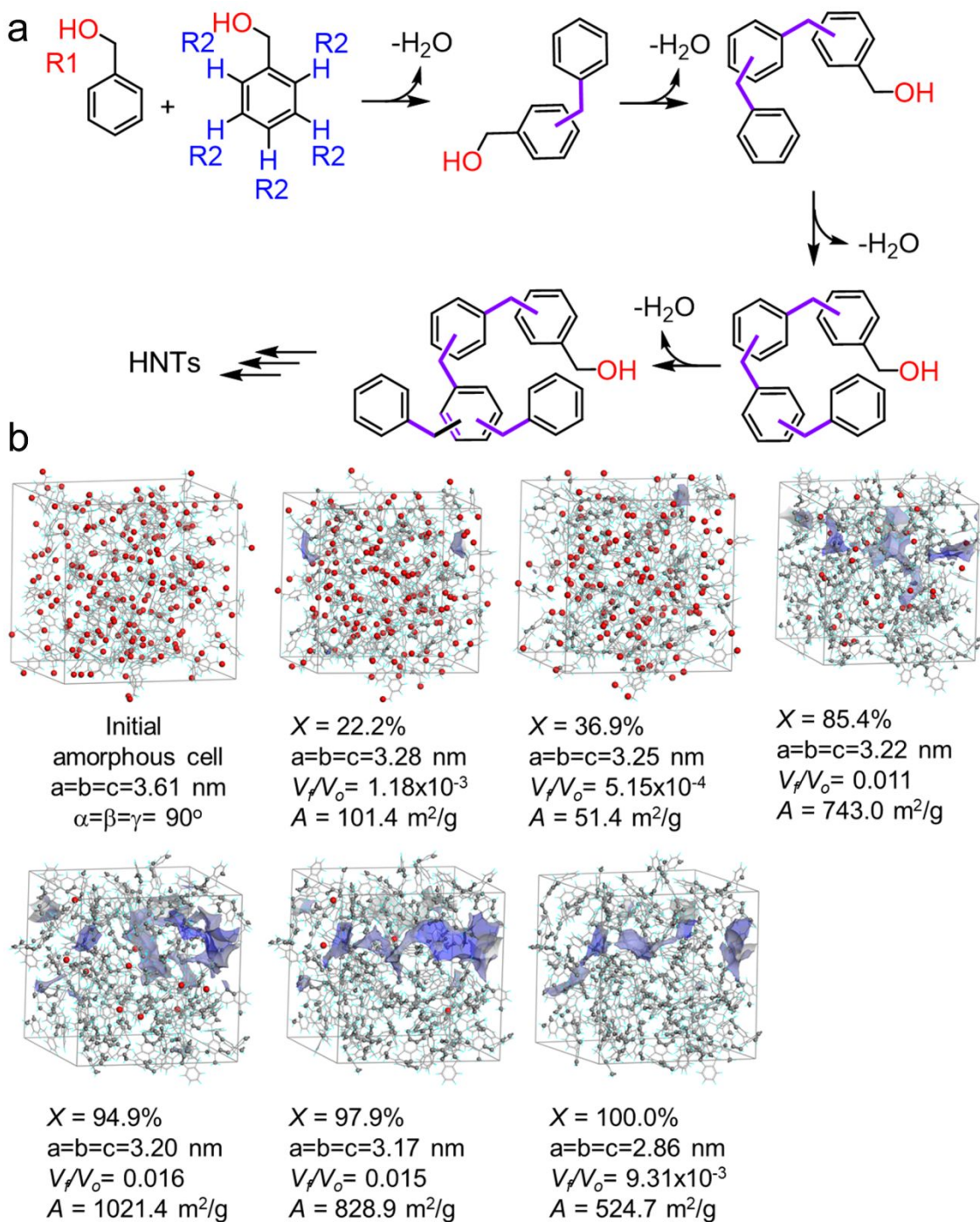**Figure S8.** Flow chart for atomic cross-linking simulations embedded in the "Cross-link" script of BIOVIA's Materials Studio software package.

Figure S9. Atomistic simulation of the BA based hyper-cross-linking polymer. (a) Preparation of HNTs network using benzyl-alcohol monomer, where new cross-links are formed by the reactions between R1 and R2, and (b) snapshots of molecular simulation boxes of HNTs taken at various degrees of crosslinking (X), showing the solvent-accessible surface areas (blue areas). For amorphous cells construction, 100 units monomer were used. Dark blue areas represent the micropore surface and grey balls and sticks represent newly formed crosslink sites.
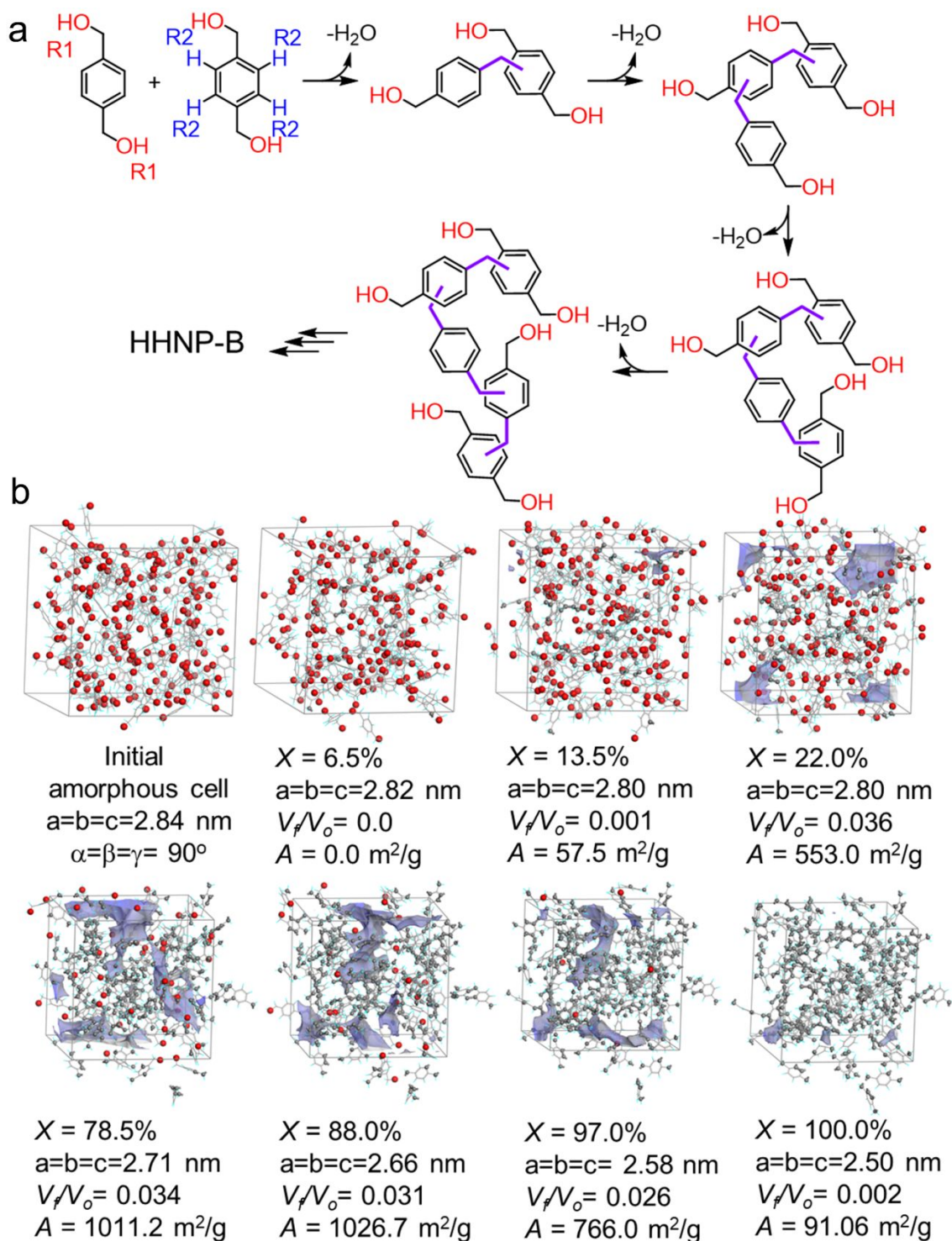
Figure S10. Atomistic simulation of the BDM based hyper-cross-linking polymer. (a) Preparation of HHNP-B network using 1,4-benzenedimethanol monomer, where new cross-links are formed by the reactions between R1 and R2, and (b) snapshots of molecular simulation boxes of HHNP-B taken at various degrees of crosslinking (X), showing the solvent-accessible surface areas (blue areas). For amorphous cells construction, 100 units monomer were used. Dark blue areas represent the micropore surface and grey balls and sticks represent newly formed crosslink sites.
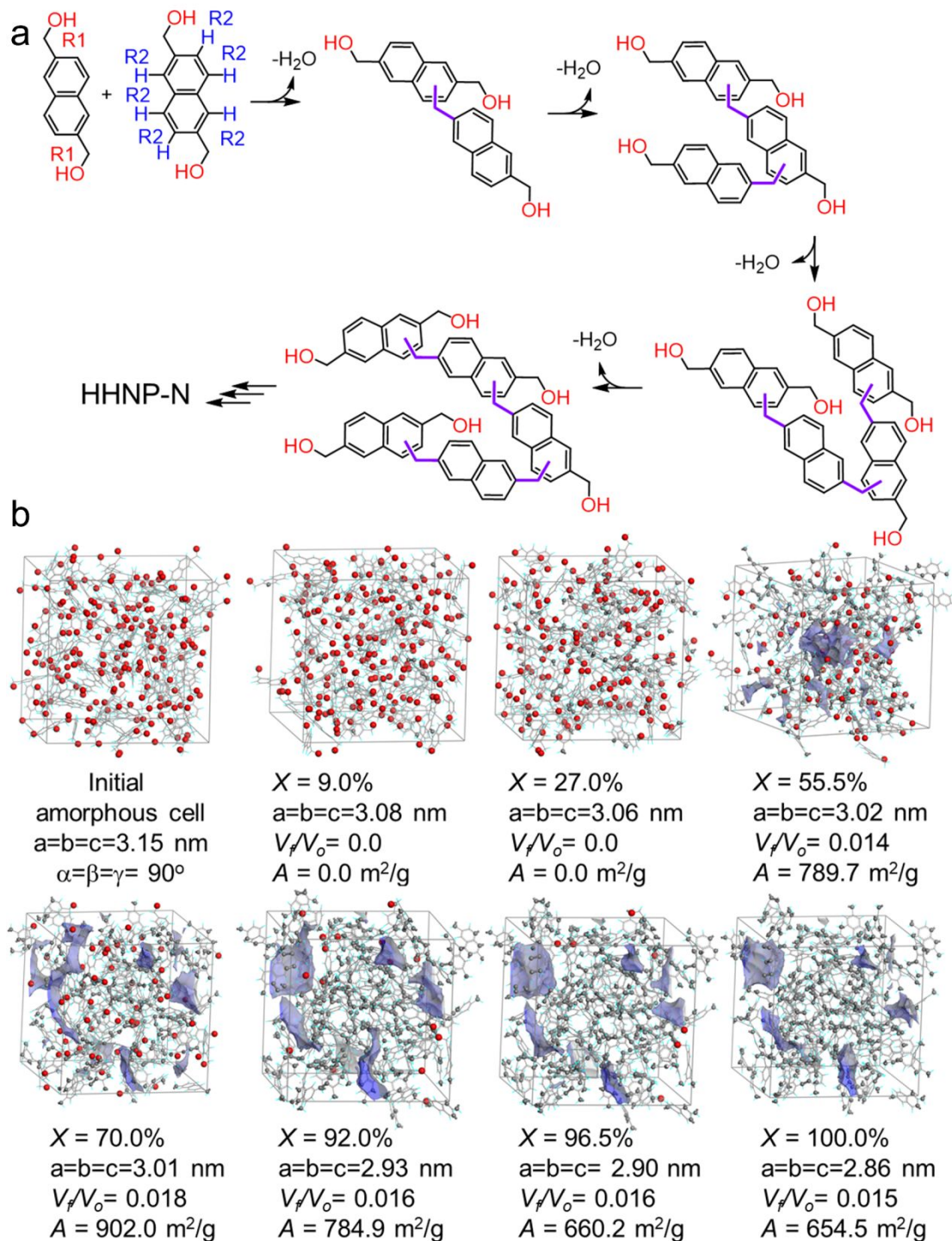
Figure S11. Atomistic simulation of the NDM based hyper-cross-linking polymer. (a) Preparation of HHNP-N network using 2,6-napahtlenedimethanol monomer, where new cross-links are formed by the reactions between R1 and R2, and (b) snapshots of molecular simulation boxes of HHNP-N taken at various degrees of crosslinking (X), showing the solvent-accessible surface areas (blue areas). For amorphous cells construction, 100 units monomer were used. Dark blue areas represent the micropore surface and grey balls and sticks represent newly formed crosslink sites.
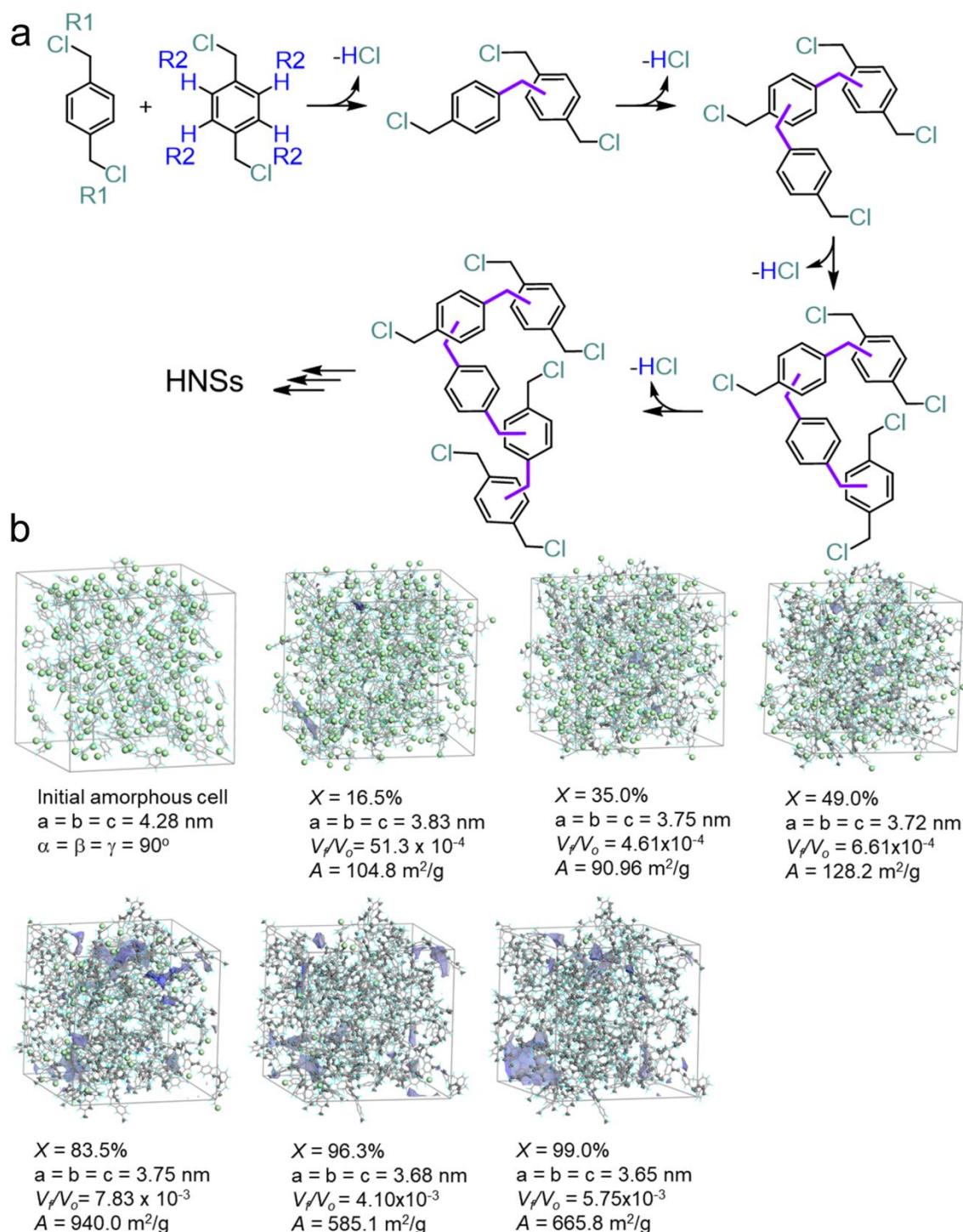
Figure S12. Atomistic simulation of the BCB based hyper-cross-linking polymer. (a) Preparation of HNSs network using 1,4-bis(chloromethyl)benzene monomer, where new cross-links are formed by the reactions between R1 and R2, and (b) snapshots of molecular simulation boxes of HHNP-N taken at various degrees of crosslinking (X), showing the solvent-accessible surface areas (blue areas). For amorphous cells construction, 100 units monomer were used. Dark blue areas represent the micropore surface and grey balls and sticks represent newly formed crosslink sites.
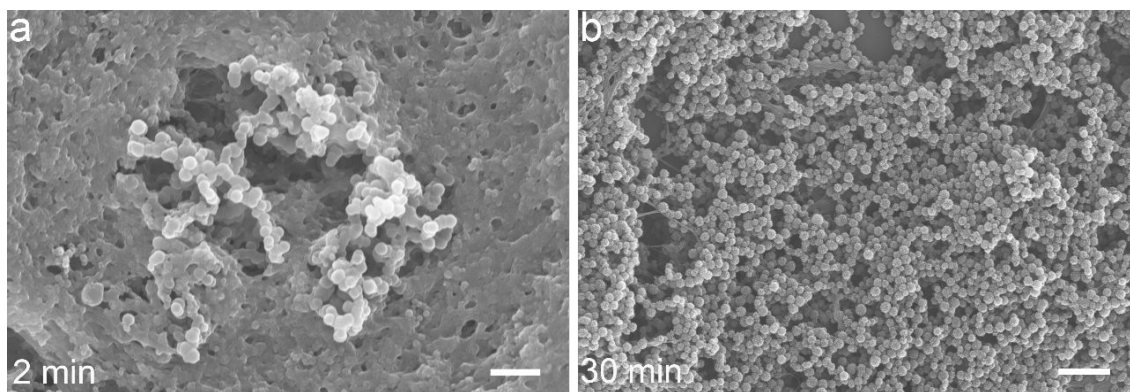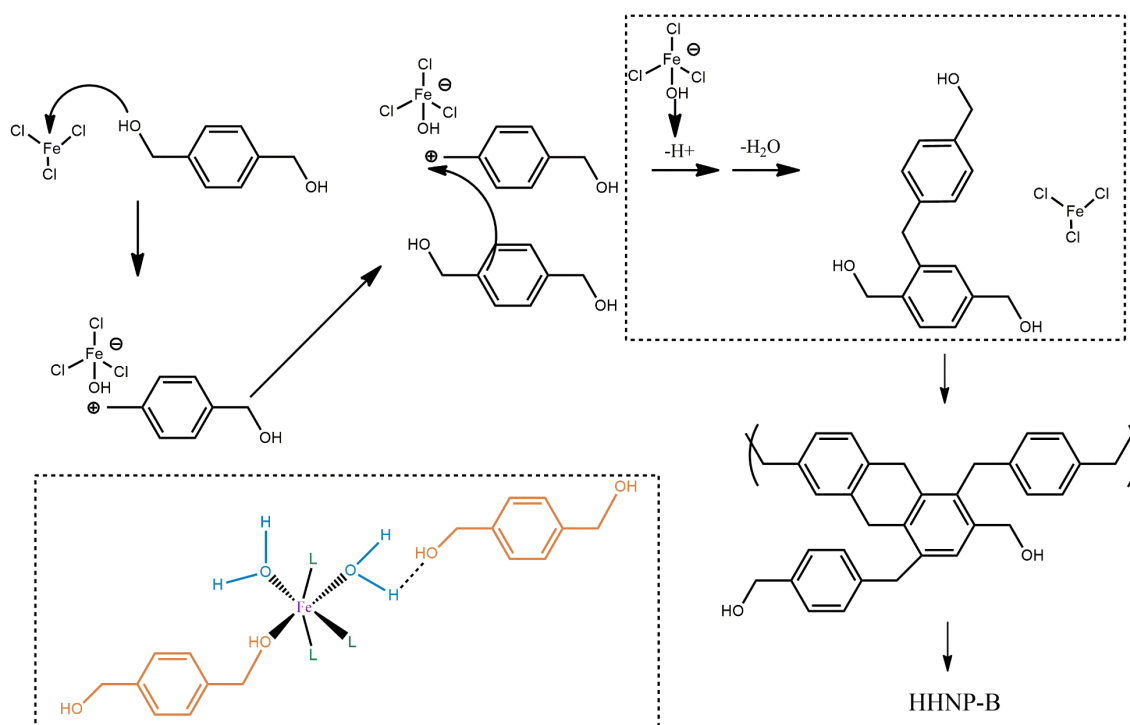
Figure S13. SEM images of the 1,4benzenedimethanol based products with various Friedel-Crafts reaction times for HHNP-B. The nanospheres is come from the slightly cross-linked polymer intermediate as evidenced by (a) SEM images in around 2 min and the hollow polymer spheres are almost formed after around 30 min as evidenced by (b) SEM images. Scale bars: 1 µm.

Figure S14. The hypothetic mechanism for form the HHNP-B, and the hydrogen bond forming between the Lewis acid and base, which will effectively balance the interaction between the monomer and catalyst. L represents either a ligand coordinated to iron or a vacant coordination site of iron.
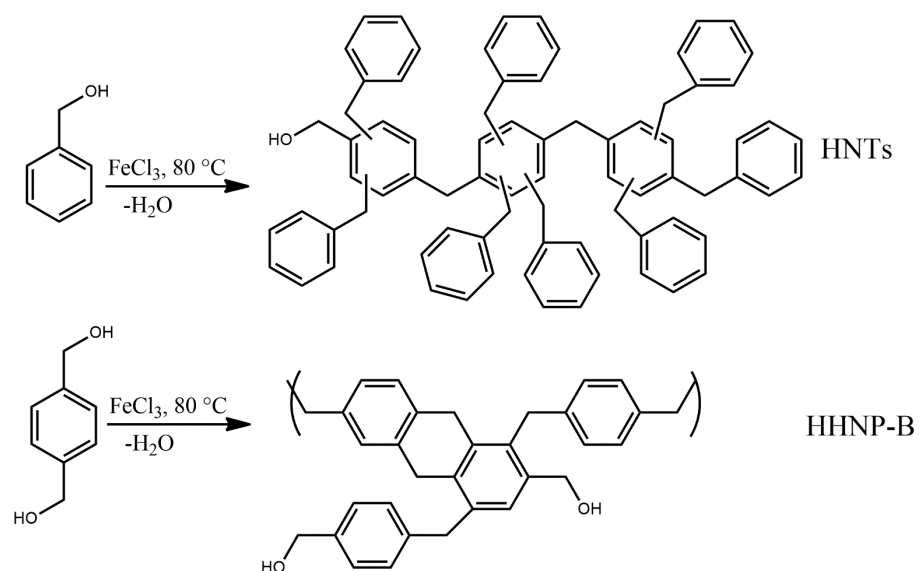
Figure S15. The possible polymeric fragments of HNTs and HHNP-B from the BA and BDM monomer, respectively, showing the different chain growth route.
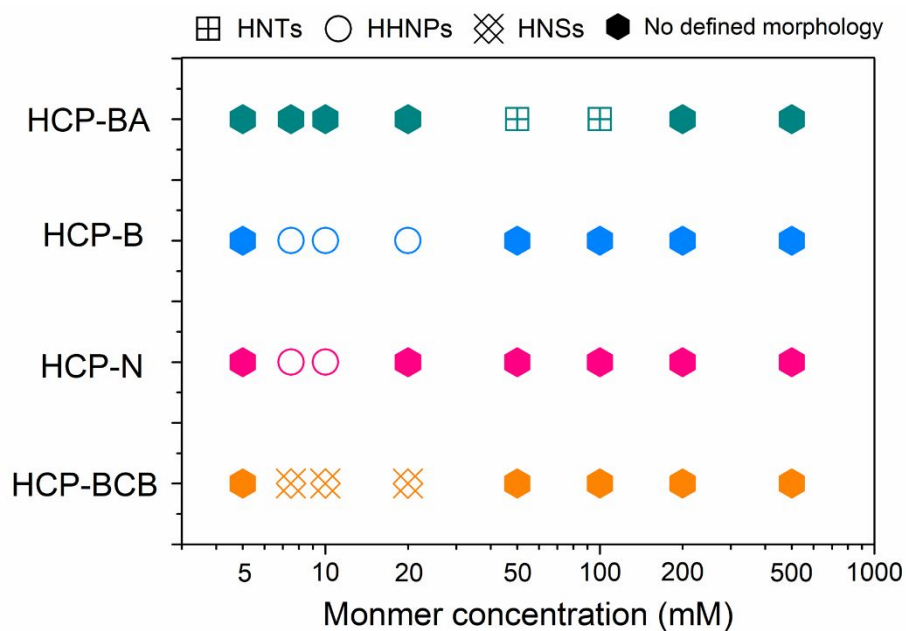
Figure S16. The morphological phase diagram of the HCP-BA, HCP-B, HCP-N, and HCP-BCB against the monomer concentration based on the experimental results.
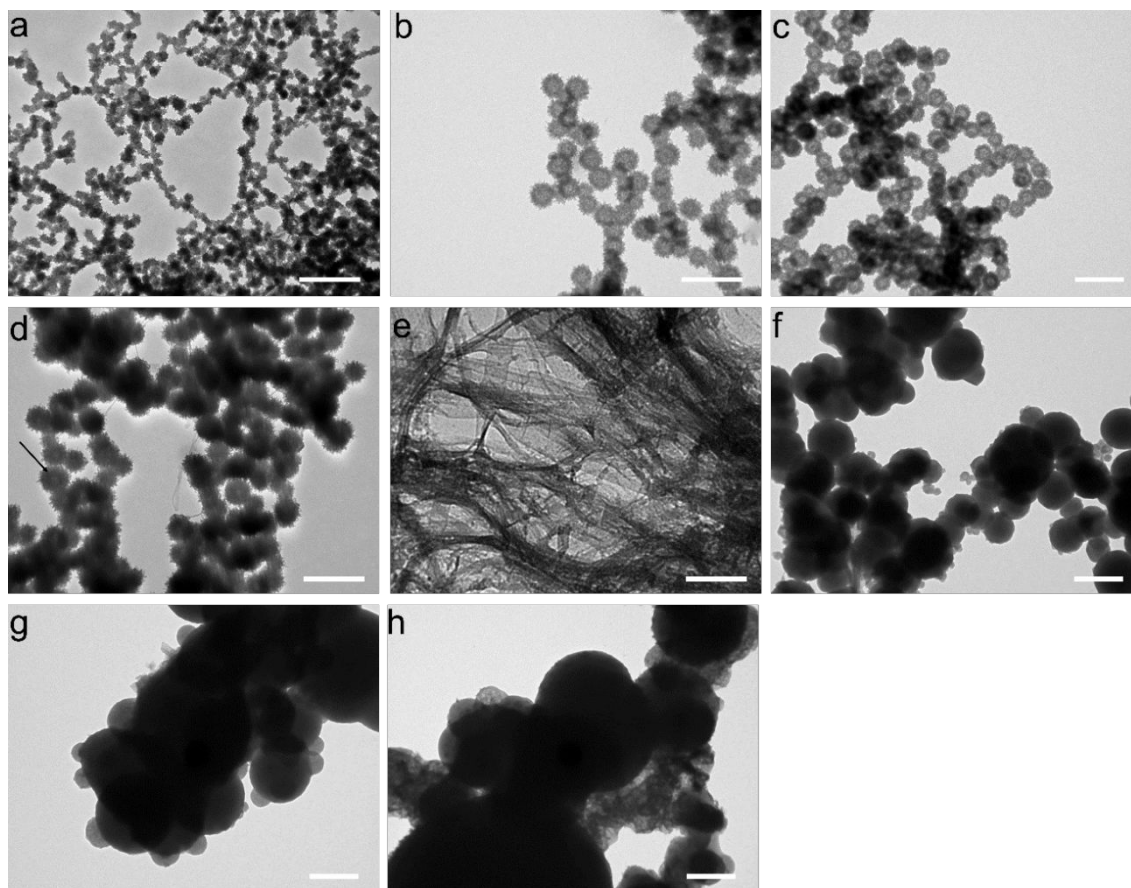
Figure S17. TEM images of the 1,4benzenedimethanol based hyper-cross-linked porous polymers with various Friedel-Crafts reaction concentrations. The self-assembled morphology evolution can be seen from the nanoworms in (a) 5 mM, hairy surface hollow polymer nanospheres in (b) 7.5 mM, (c) 10 mM, (d) 20 mM, the disordered tubes in (e) 100 mM, and the continue disordered spherical particles in (f) 200 mM, (g) 500 mM, (h) 1000 mM. The inner diameters of hollow nanospheres can be vary from around 125 nm to around 30 nm by control the monomer concentrations. Scale bars: 500 nm. The concentration is the monomer of BDM in the DCE solution.
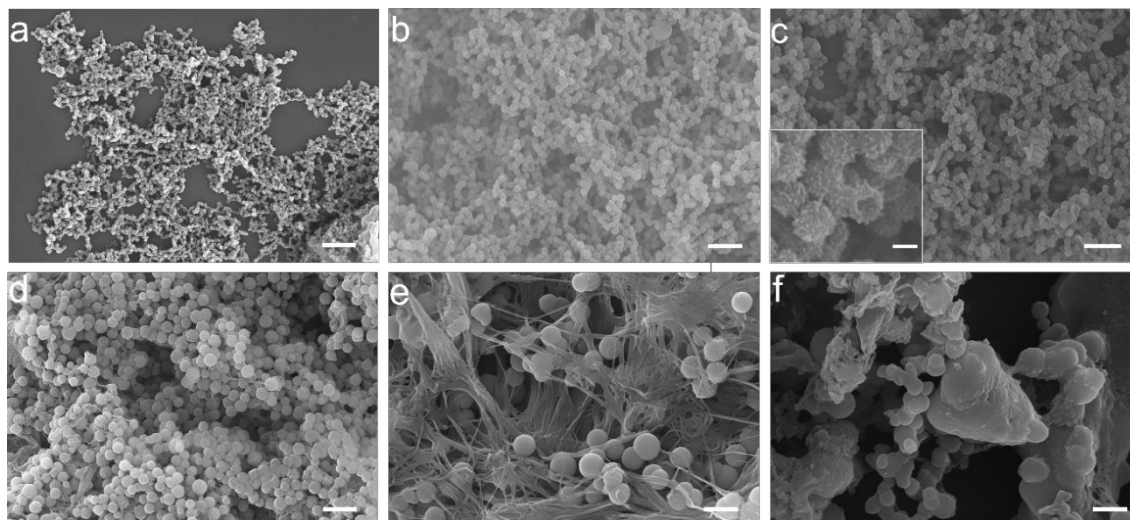
Figure S18. SEM images of the 1,4benzenedimethanol based hyper-cross-linked porous polymer with various Friedel-Crafts reaction concentrations. The self-assembled morphology evolution can be seen from the nanoworms in (a) 5 mM, polymer nanospheres with the hairy surface in (b) 7.5 mM, (c) 10 mM, (d) 20 mM, the disorder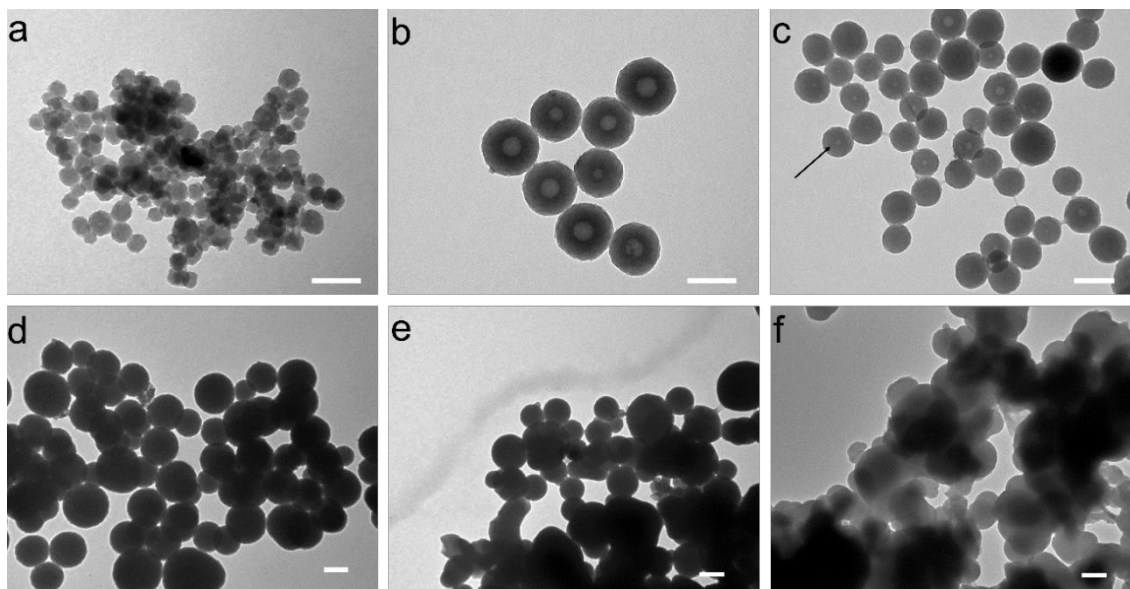ed tubes in (e) 100 mM, and the disordered spherical particles in (f) 200 mM. Scale bars: 1 µm. The inset of (c) shows the opened spheres indicating the hollow structures. Scale bar: 100 nm in the inset of c.

Figure S19. TEM images of the 2,6naphthalenedimethanol based hyper-cross-linked porous polymer with various Friedel-Crafts reaction concentrations. The self-assembled morphology evolution can be seen from the spherical particles in (a) 5 mM, smooth surface hollow polymer nanospheres in (b) 7.5 mM, (c) 10 mM, the solid spheres in (d) 20 mM, and the continue disordered spherical particles in (e) 200 mM, (f) 500 mM. The inner diameters of hollow nanospheres can be vary from around 85 nm to around 30 nm by control the monomer concentration. Scale bars: 200 nm.
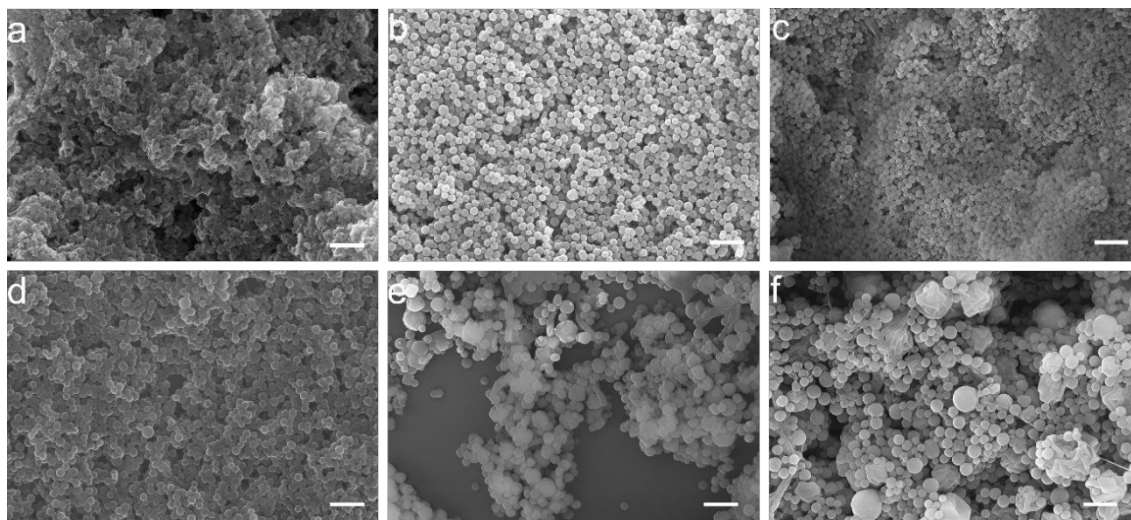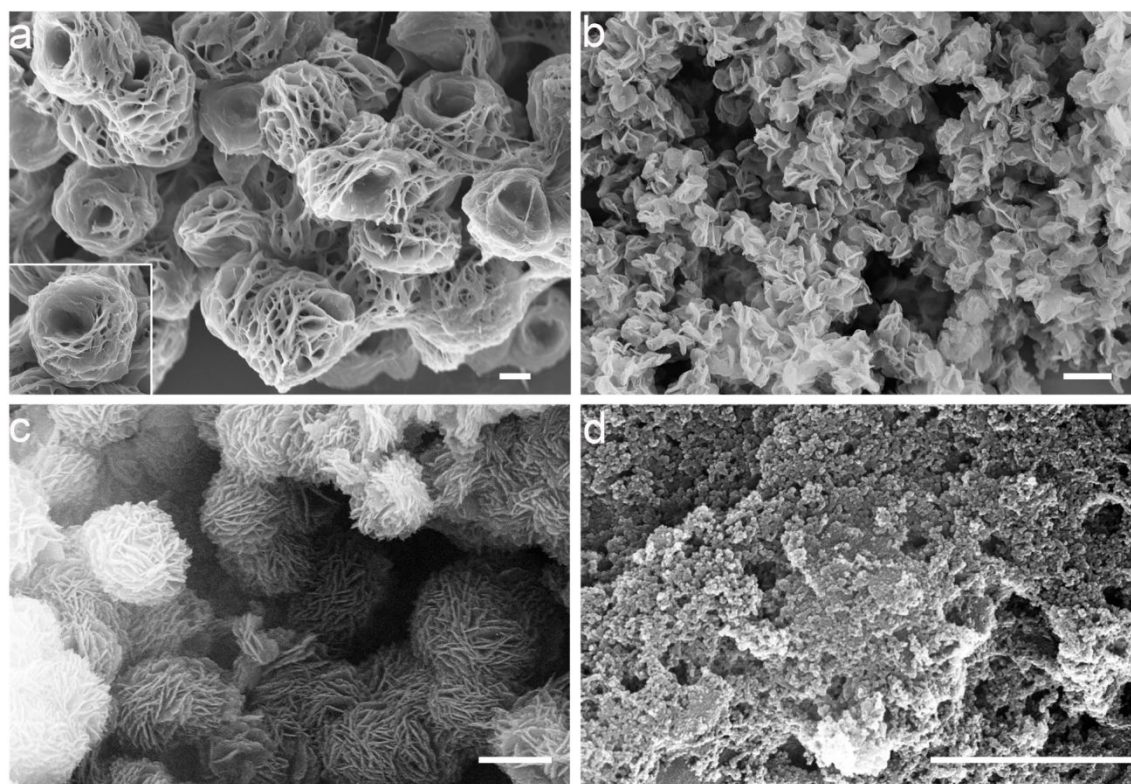
Figure S20. SEM images of the 2,6naphthalenedimethanol based hyper-cross-linked porous polymer with various Friedel-Crafts reaction concentrations. The self-assembled morphology evolution can be seen from the spherical particles in (a) 5 mM, smooth surface polymer nanospheres in (b) 7.5 mM, (c) 10 mM, (d) 20 mM, and the continue disordered spherical particles in (e) 100 mM, (f) 200 mM. Scale bars: 1 μm.

Figure S21. SEM images of the 1,4-bis(chloromethyl)benzene based hyper-cross-linked porous polymer with various Friedel-Crafts reaction concentrations. The self-assembled morphology evolution can be seen from the flower-like shape in (a) 5 mM, nanosheet in (b) 20 mM, nanoflake in (c) 100 mM, and the disordered spherical particles in (d) 500 mM. Scale bars: 1 μm.
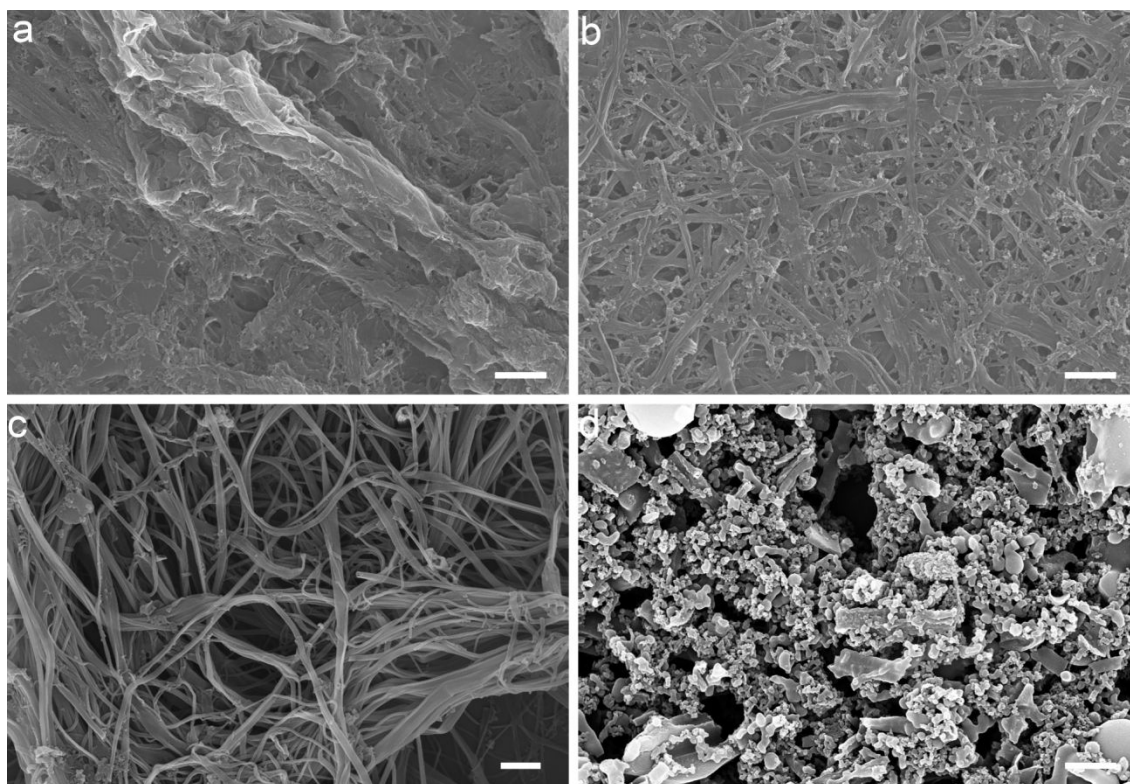
Figure S22. SEM images of the benzyl alcohol based hyper-cross-linked porous polymer with various Friedel-Crafts reaction concentrations. The self-assembled morphology evolution can be seen from the nanoparticles in (a) 5 mM, fiber and particles in (b) 10 mM, nanotube in (c) 100 mM, and the disordered spherical particles in (d) 500 mM. Scale bars: 1 μm.
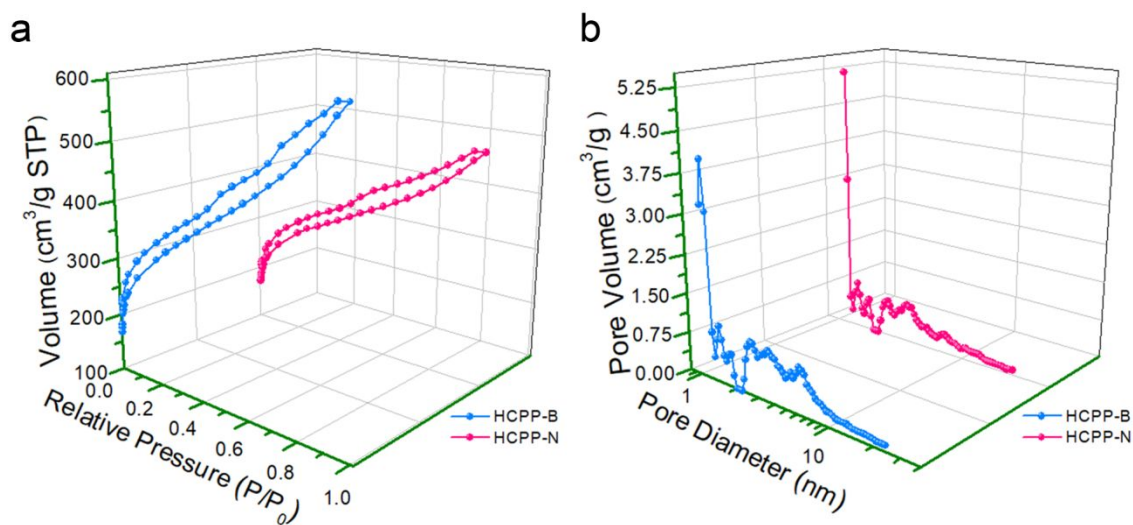
Figure S23. Surface area and pore size measurement of HCPPs. The nitrogen adsorption/desorption isotherms of HCPP-B and HCPP-N (a), pore size distributions for HCPP-B and HCPP-N (b).

17
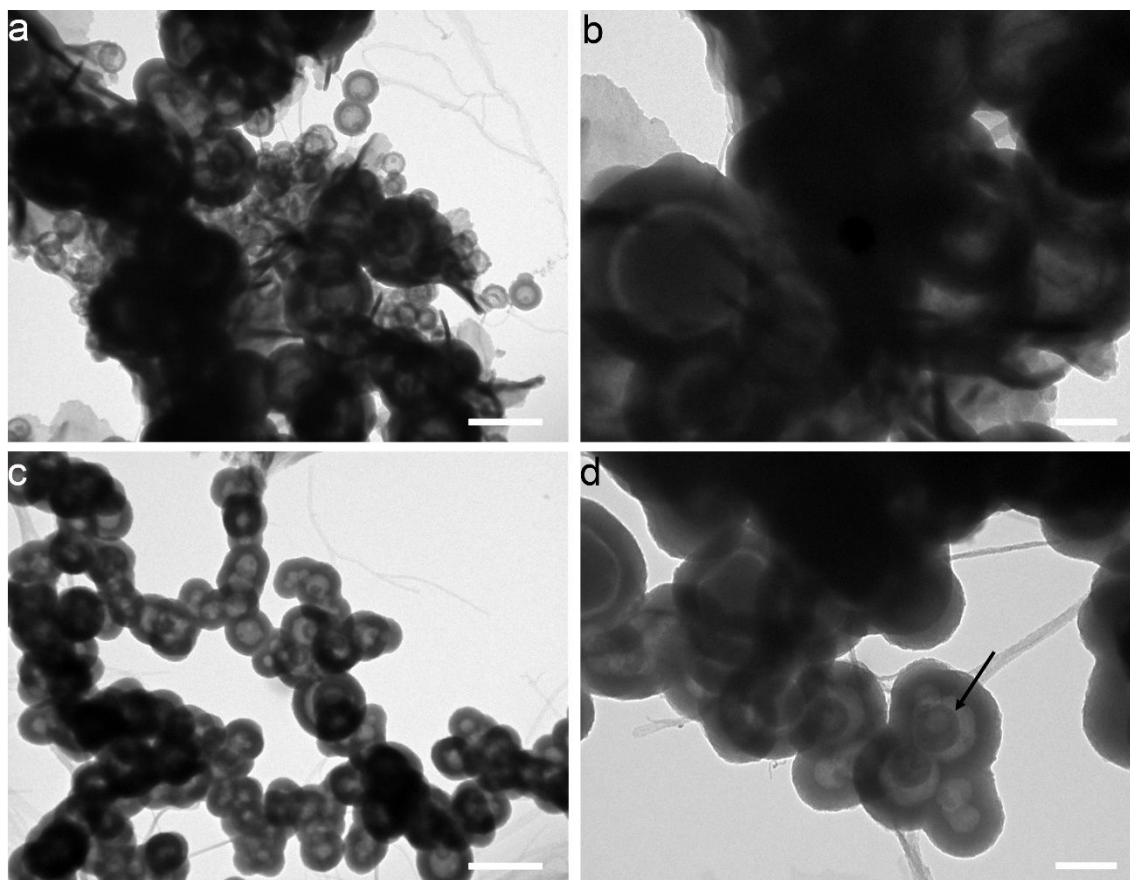
Figure S24. TEM images of the 1,4benzenedimethanol based hyper-cross-linked porous polymer with different Friedel-Crafts reaction temperatures. The non-uniform hollow and solid polymer clusters could be observed in 25 ℃ (a), (b), and the relative uniformed, multiply stacked hole spheres could be observed in 50 ℃ (c), (d). It can be seen that the multishelled hollow nanospheres in the (d), showing the potential on design inner constitutional styles by LAB interaction-mediated self-assembly method. It also can be seen that spheres with smooth surface are formed in the low temperature condition, indicating that temperature is important for the formation of the hairy surface. Scale bars: 500 nm in a, c, and 200 nm in b, d.
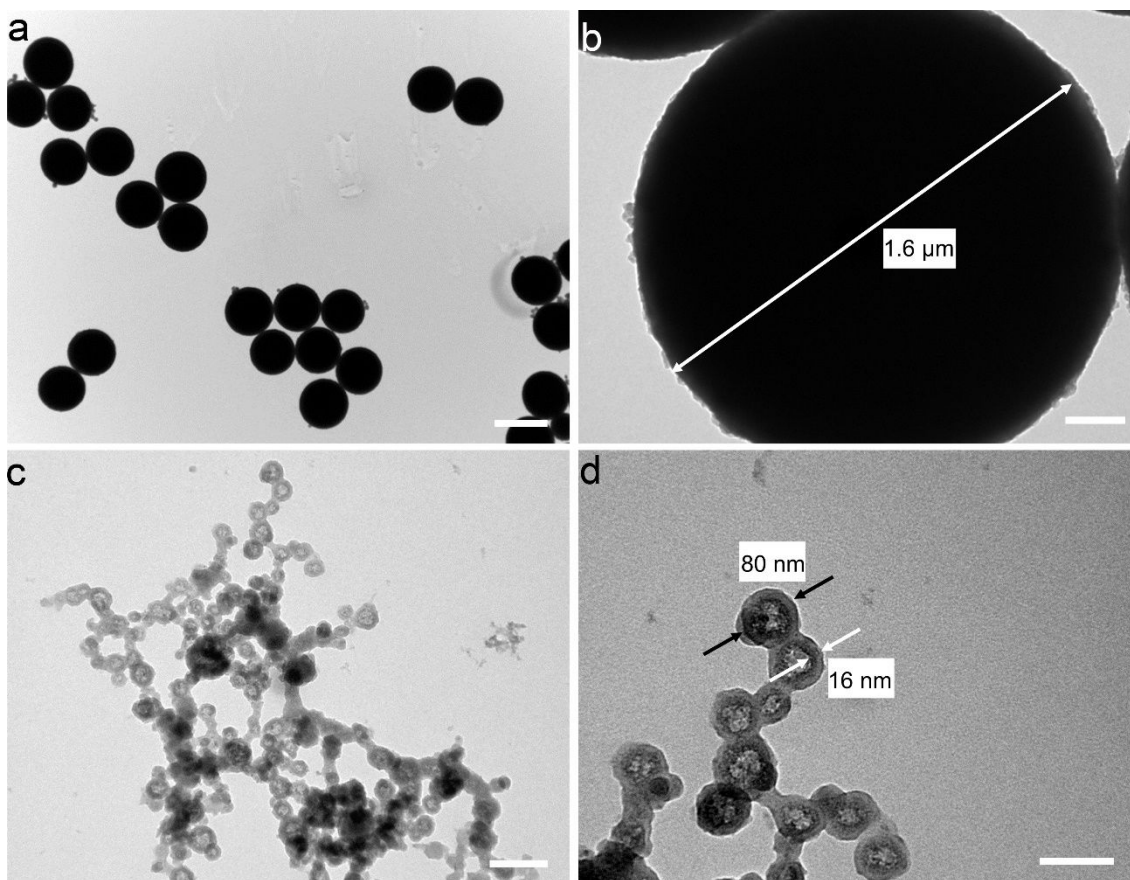
Figure S25. TEM images of the 1,4benzenedimethanol based hyper-cross-linked porous polymer with different Friedel-Crafts reaction catalysts. The biggish solid polymer spheres can be seen from the $SnCl_4$ catalyzed polymerization (a), (b), the average diameter is about 1.6 µm for the solid sphere. The hollow polymer nanospheres can be seen from the $AlCl_3$ catalyzed polymerization (c), (d), the sizes of hollow spheres are smaller than the HHNPs obtained from the $FeCl_3$ catalyzed polymerization, indicating the hollow size can be tailored by change the catalyst. Scale bars: 2 µm in a, 200 nm in b, c, and 100 nm in d.
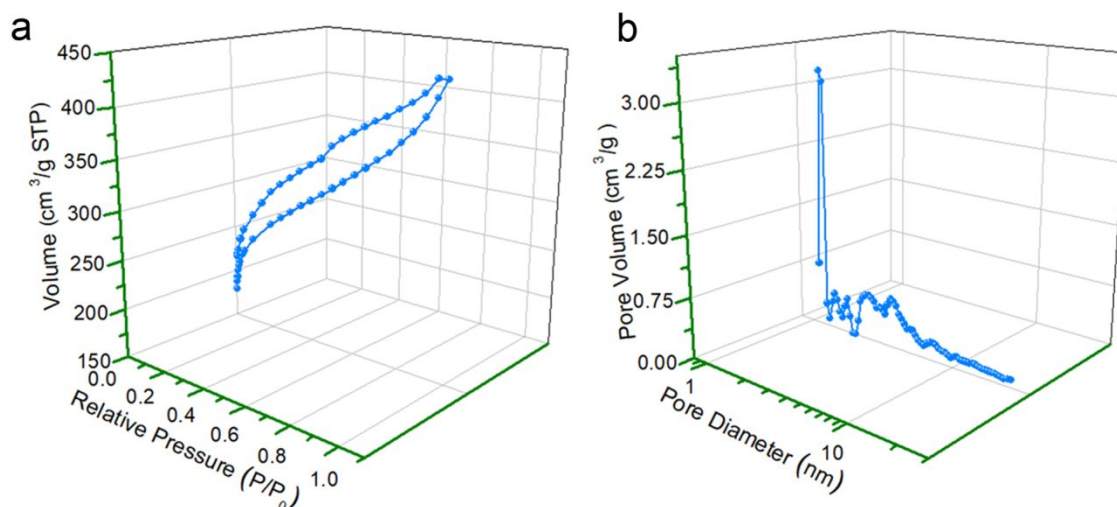
Figure S26. Characterizations of 1,4benzenedimethanol based hyper-cross-linked porous hollow polymer spheres using concentrated H_2SO_4 (SA-HHNP-B) at identify conditions. (a) The nitrogen adsorption/desorption isotherms of SA-HHNP-B, and (b) pore size distributions calculated by nonlocal density functional theory (NL-DFT) for SA-HHNP-B.
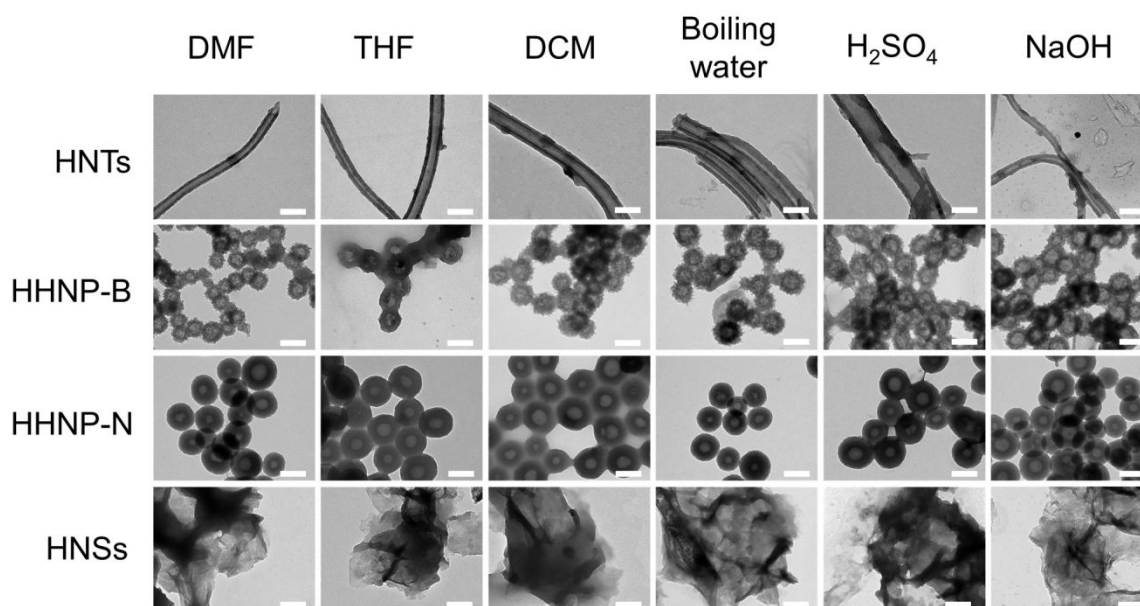
Figure S27. TEM images of the HCPs after the treatment under different harsh conditions (DMF, THF, DCM, Boiling water, concentrated H_2SO_4 (18 M), and saturated NaOH (14 M) for one week. It can be seen that the nanotubes, hollow nanospheres, and nanosheets still exist and without distinctively damage from its origin morphology.
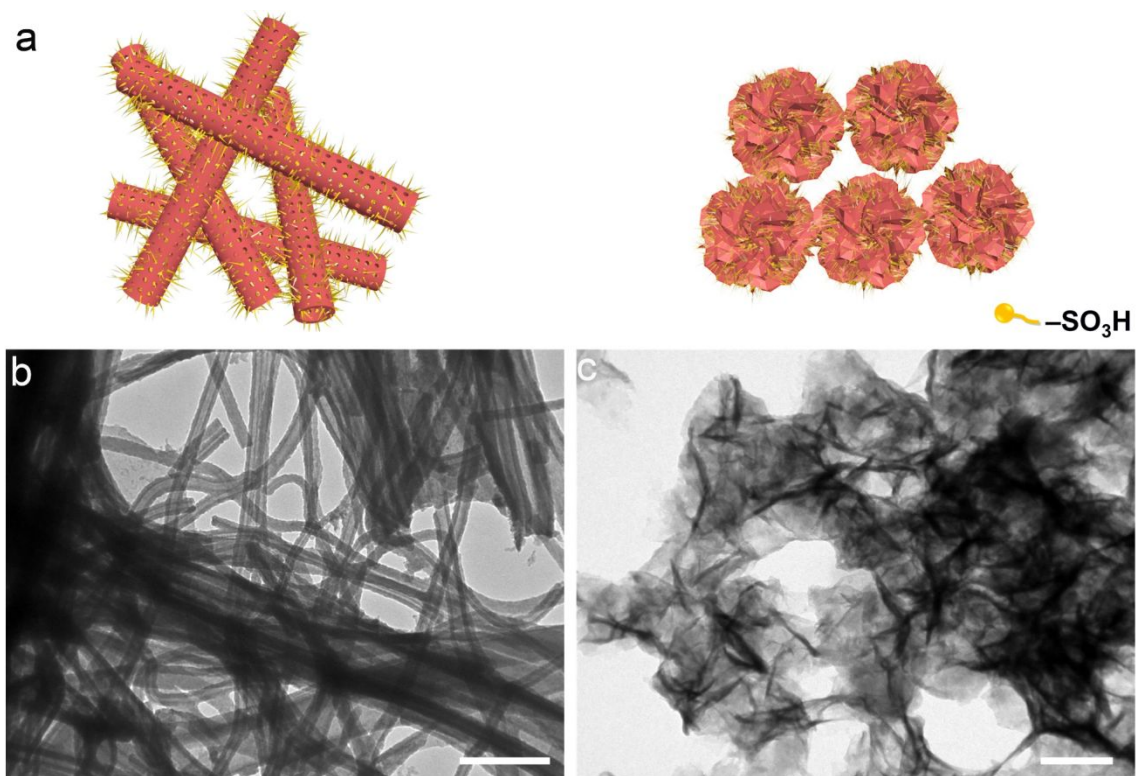
Figure S28. The TEM images of the sulfonic acid-functionalized nanotubes and nanosheets. (a) Schematic illustration of the SNTs and SNSs. The TEM images of (b) SNTs, (c) SNSs. Scale bars: 500 nm
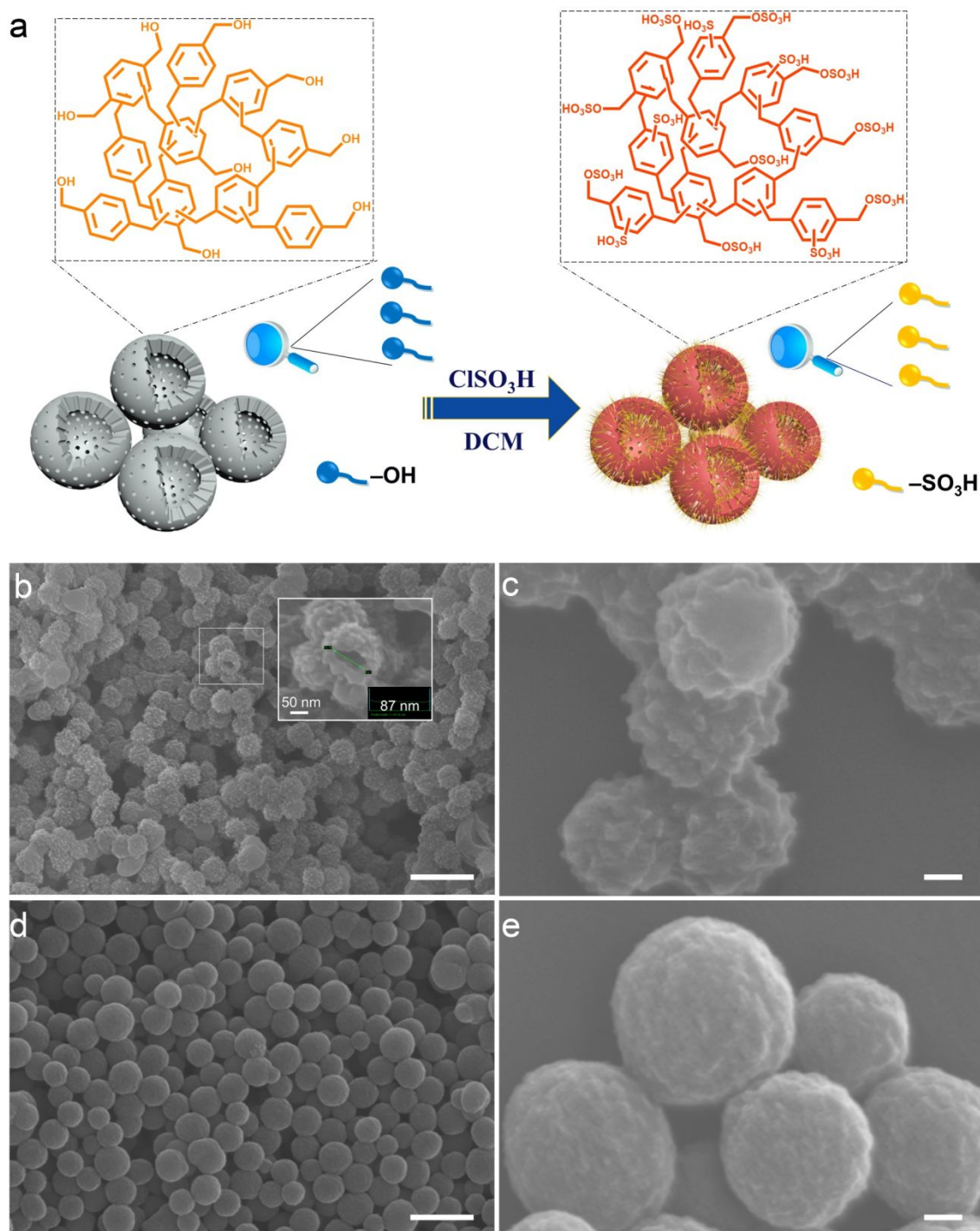
Figure S29. The SEM images of the sulfonic acid-functionalized hollow polymer nano-spheres (SHNPs). (a) Schematic of the synthetic path for the SHNPs. The SEM images of (b), (c) SHNP-B, (d), (e) SHNP-N. Inset of (b) shows the selected SHNP-B with around 87 nm inner hole diameter, indicating the hollow structures remain after the rough sulfonic acid functionalization process. The slightly damage on the surface topology of HHNPs after the sulfonation process can be observed in the (c) and (e). Scale bars: 500 nm in b, d, and 50 nm in c, e.
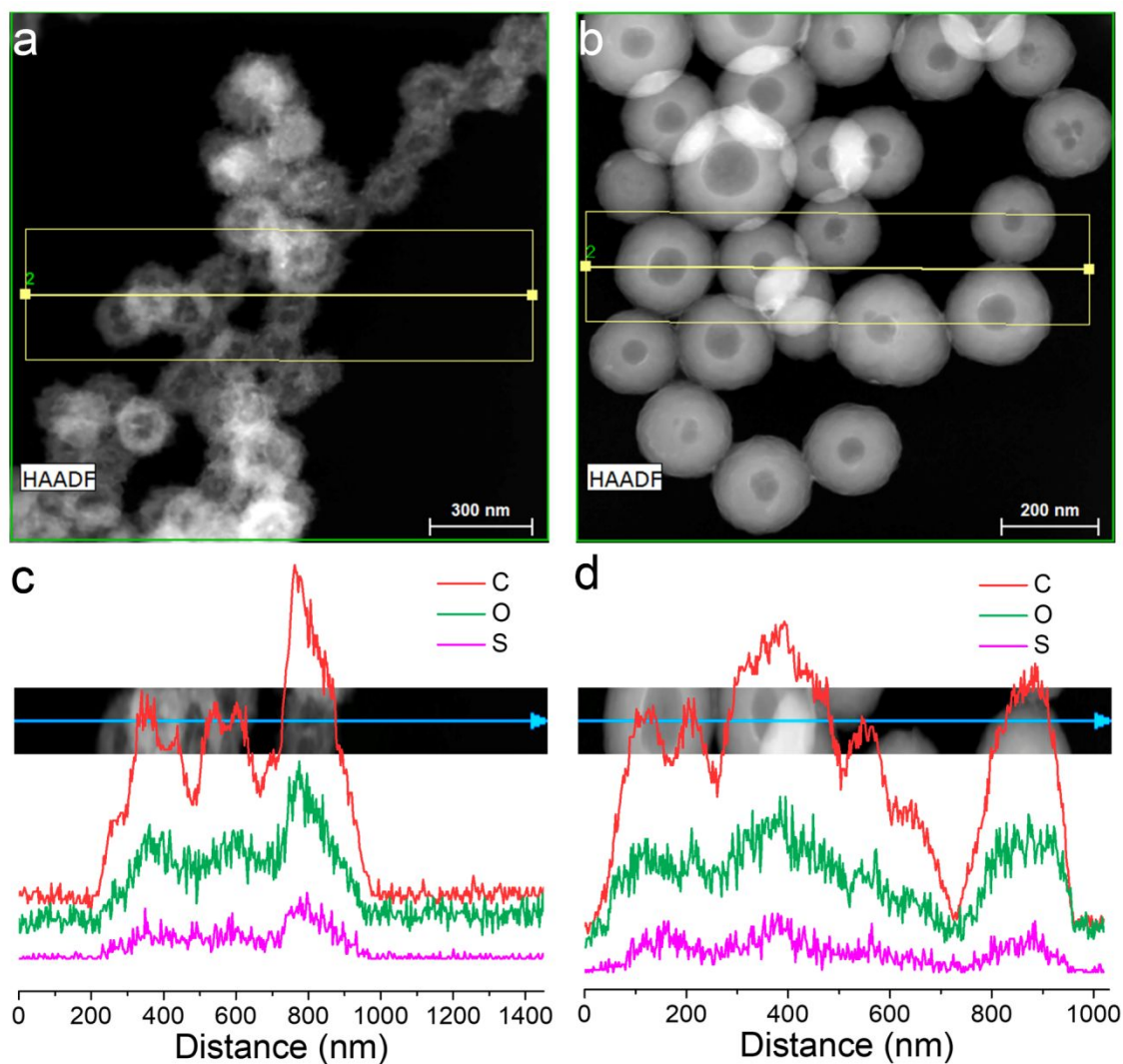
Figure S30. High-angle annular dark field scanning transmission electron microscopy (HAADF-STEM) images and EDS line scan images of the SHNP-B and SHNP-N. The results of (a, c) SHNP-B and (b, d) SHNP-N, showing the hollow structures are keep well after the hazardous sulfonation process.
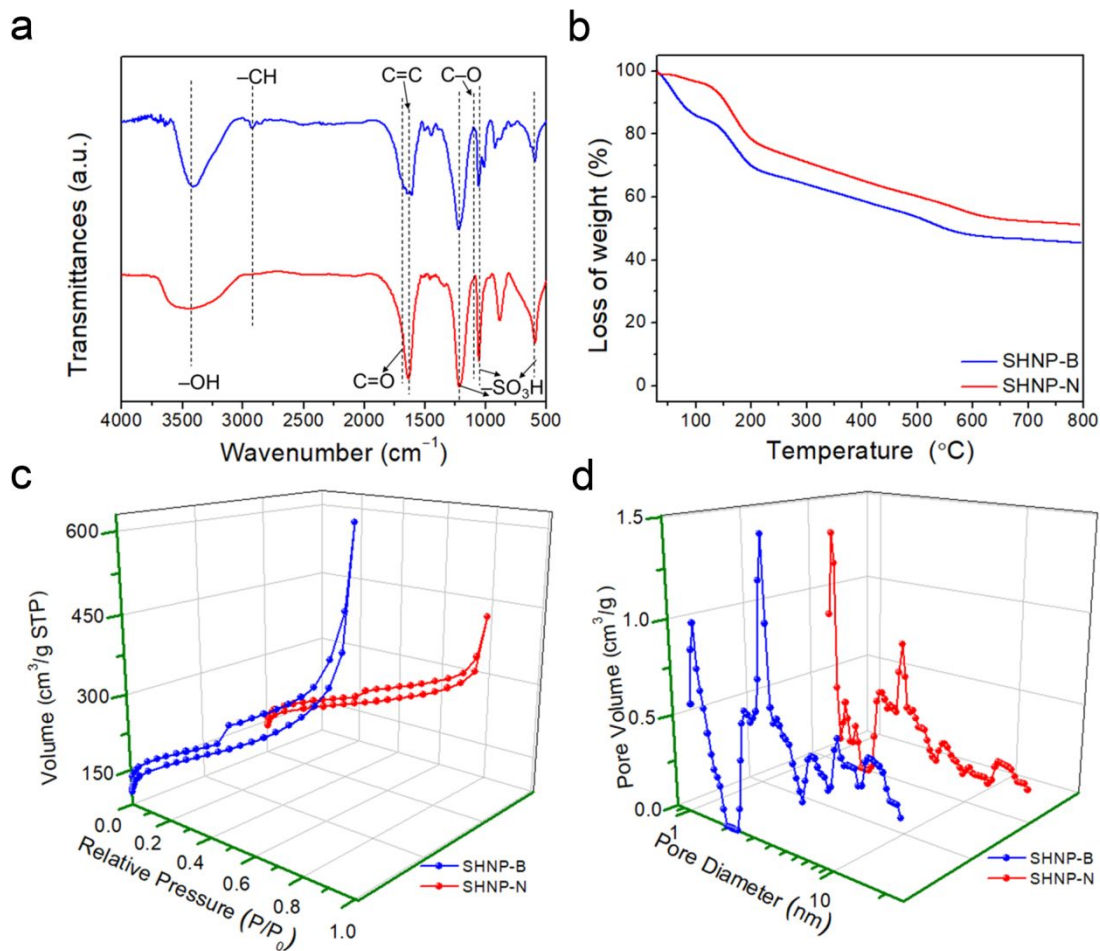
Figure S31. Structural analysis of SHNPs. (a) FT-IR analysis of the SHNP-B and SHNP-N, SHNP-B (upper) and SHNP-N (lower). (b) TGA analysis of the SHNP-B and SHNP-N under N_2 atmospheres. (c) Nitrogen adsorption and desorption isotherms at 77.3 K of the SHNP-B and SHNP-N, and (d) pore size distribution curves calculated by NL-DFT for the SHNP-B and SHNP-N.
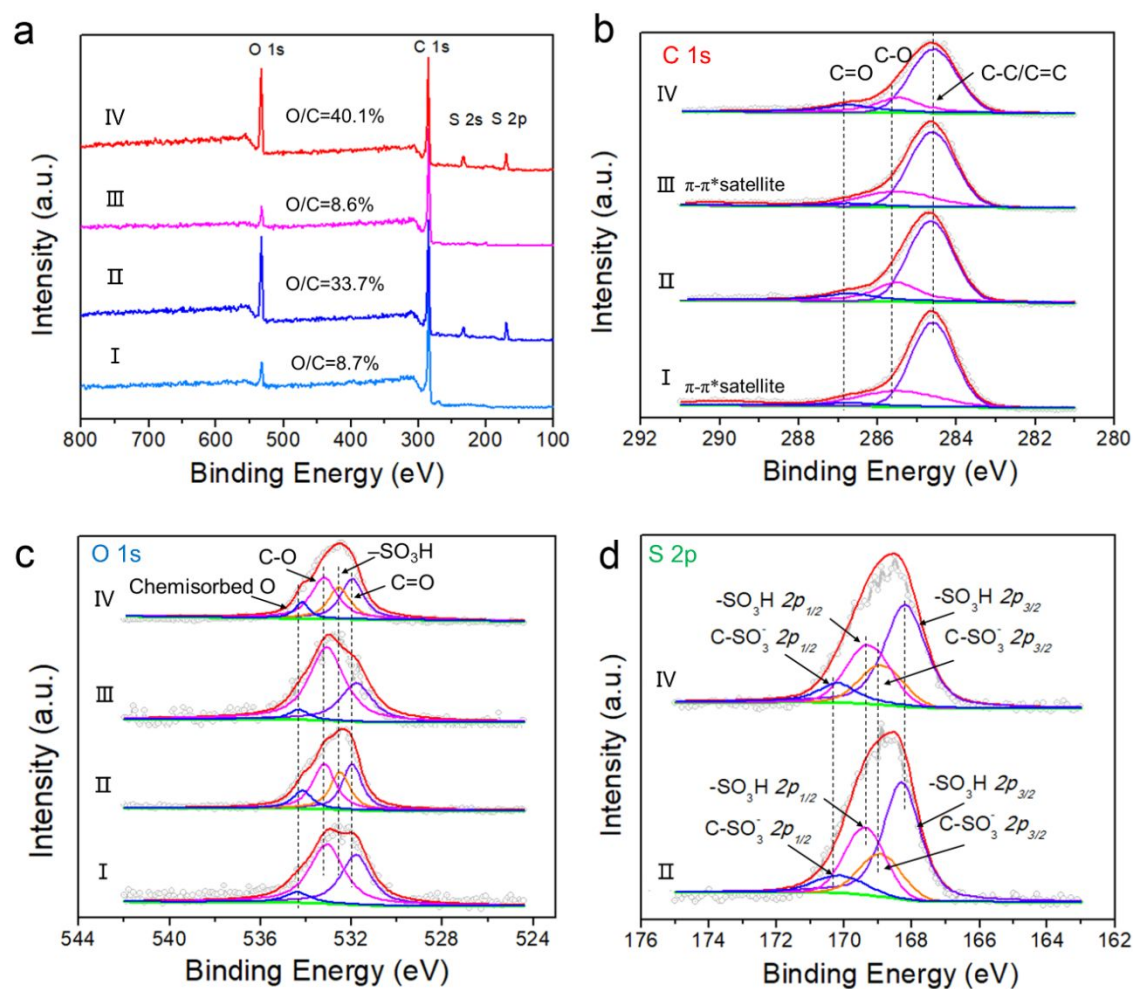
Figure S32. Comparation of the XPS spectra before and after sulfonation. (a) Survey of SHNPs and HHNPs, (b) C 1s peaks, (c) O 1s peaks, (d) S 2p peaks. (I) HHNP-B, (II) SHNP-B, (III) HHNP-N, and (IV) SHNP-N.
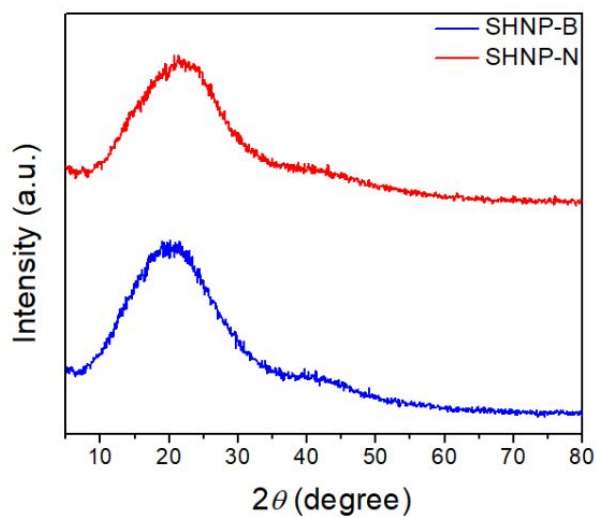
Figure S33. Powder XRD profiles for SHNP-B and SHNP-N.
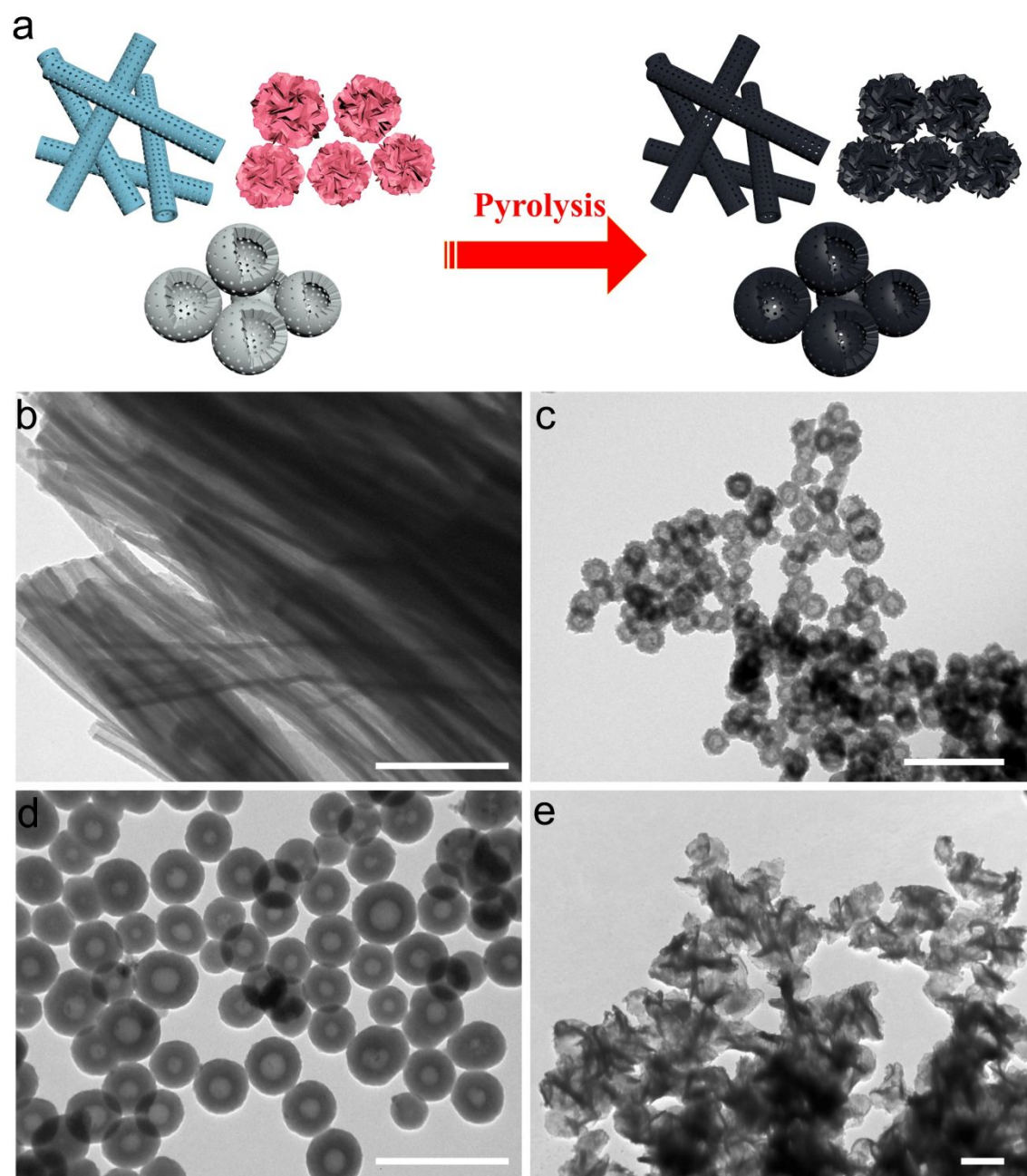
Figure S34. Morphology characterizations of carbon nanotubes, hollow carbon nano-spheres and carbon nanosheets derived from pyrolysis of corresponding polymers. (a) Schematic of the synthetic path for devise morphology-controlled carbons. The TEM images of (b) PNTs, (c) PHNP-B, (d) PHNP-N, and (e) PNSs. After carbonization, the carbons retain an original morphology without any obvious collapse of corresponding structures, and compared with the original polymers, the shell thickness of carbons become slightly smaller. Scale bars: 500 nm.
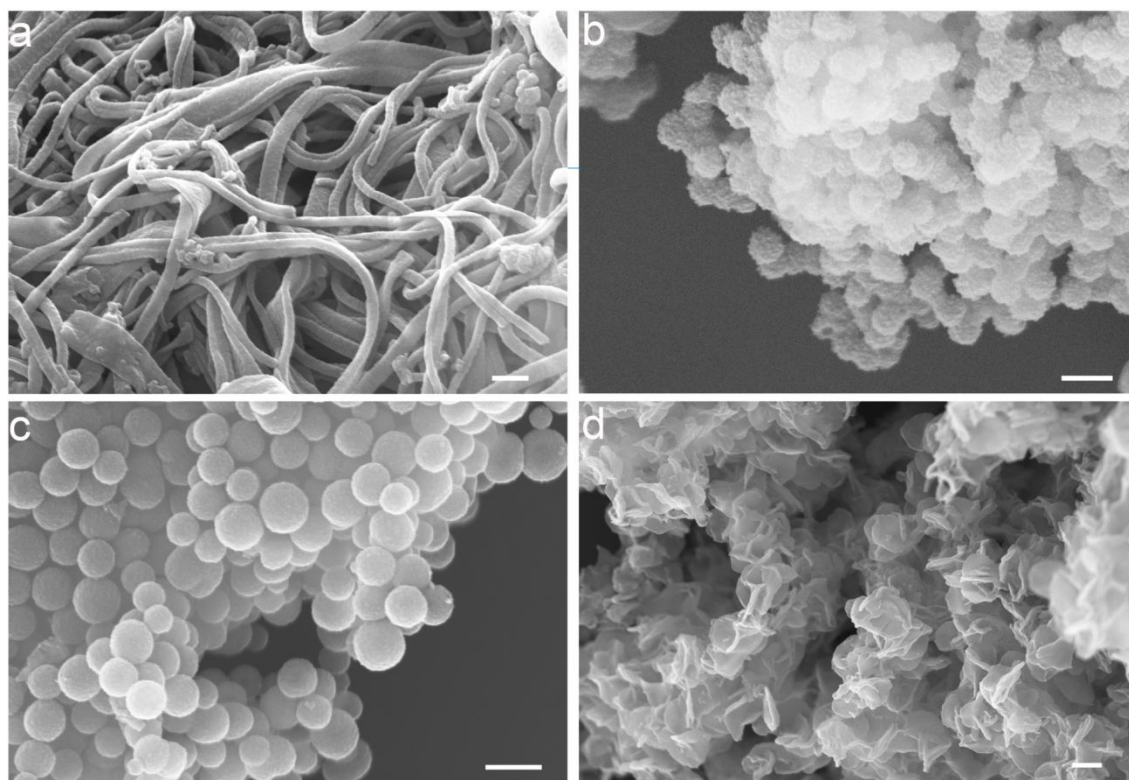
Figure S35. Morphology characterizations of carbons. The SEM images of the (a) PNTs, (b) PHNP-B, (c) PHNP-N and (d) PNSs. It can be seen that the morphologies without any obvious collapse of the original form. The SEM images show the 3D stacked hierarchical carbon nanotubes, 3D stacked hollow carbon nanospheres and 3D stacked carbon nanosheets. Scale bars: 250 nm.
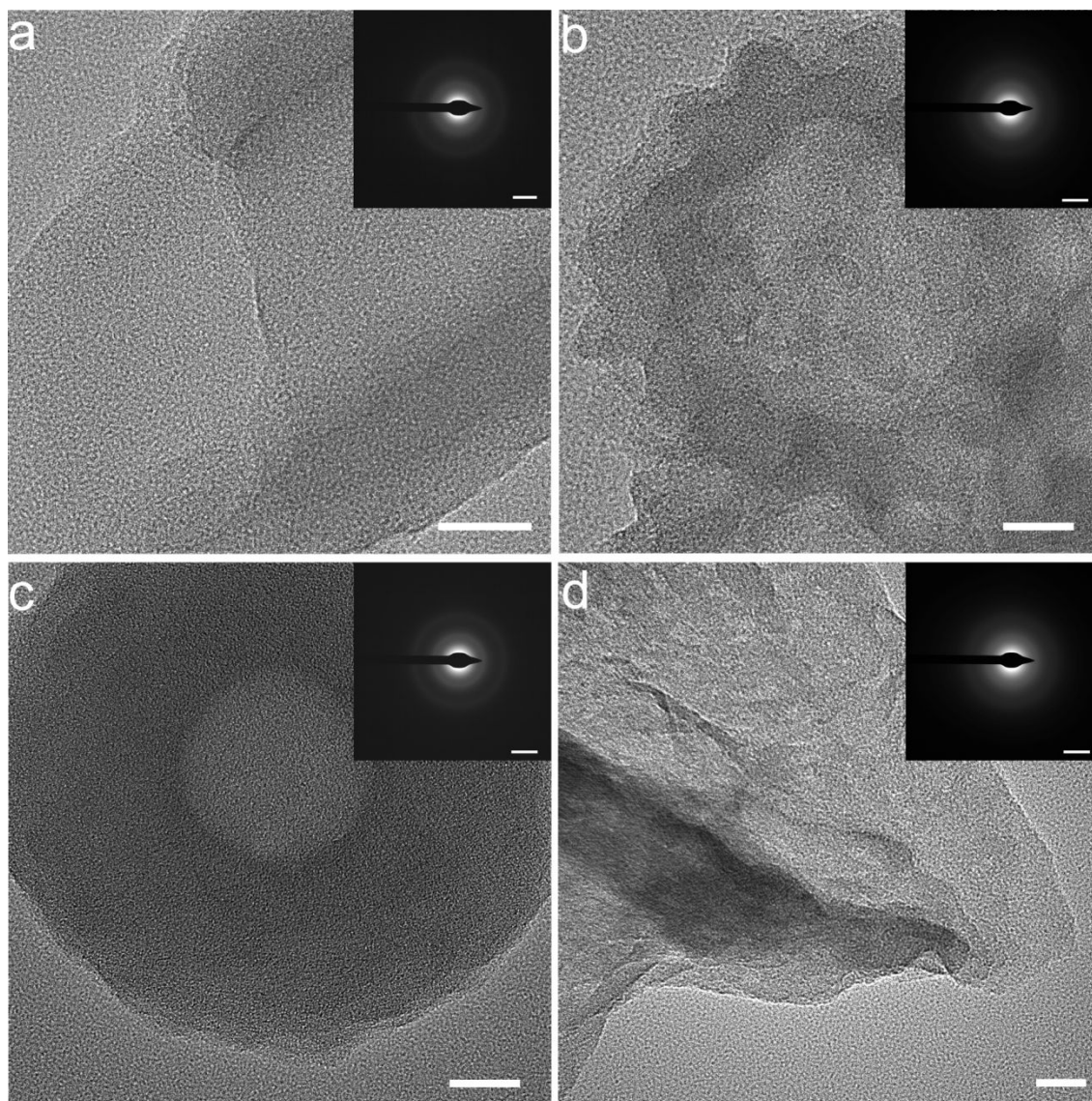
Figure S36. Morphology characterizations of carbons. The HR-TEM images of the (a) PNTs, (b) PHNP-B, (c) PHNP-N and (d) PNSs, the visible micro/meso pores exist on the walls of the carbon nanotubes, the shells of the hollow carbon nanospheres, and the edges of the carbon nanosheets. The insets of (a-d) show the corresponding SAED patterns. Scale bars: 20 nm, and 5 1/nm in the insets.
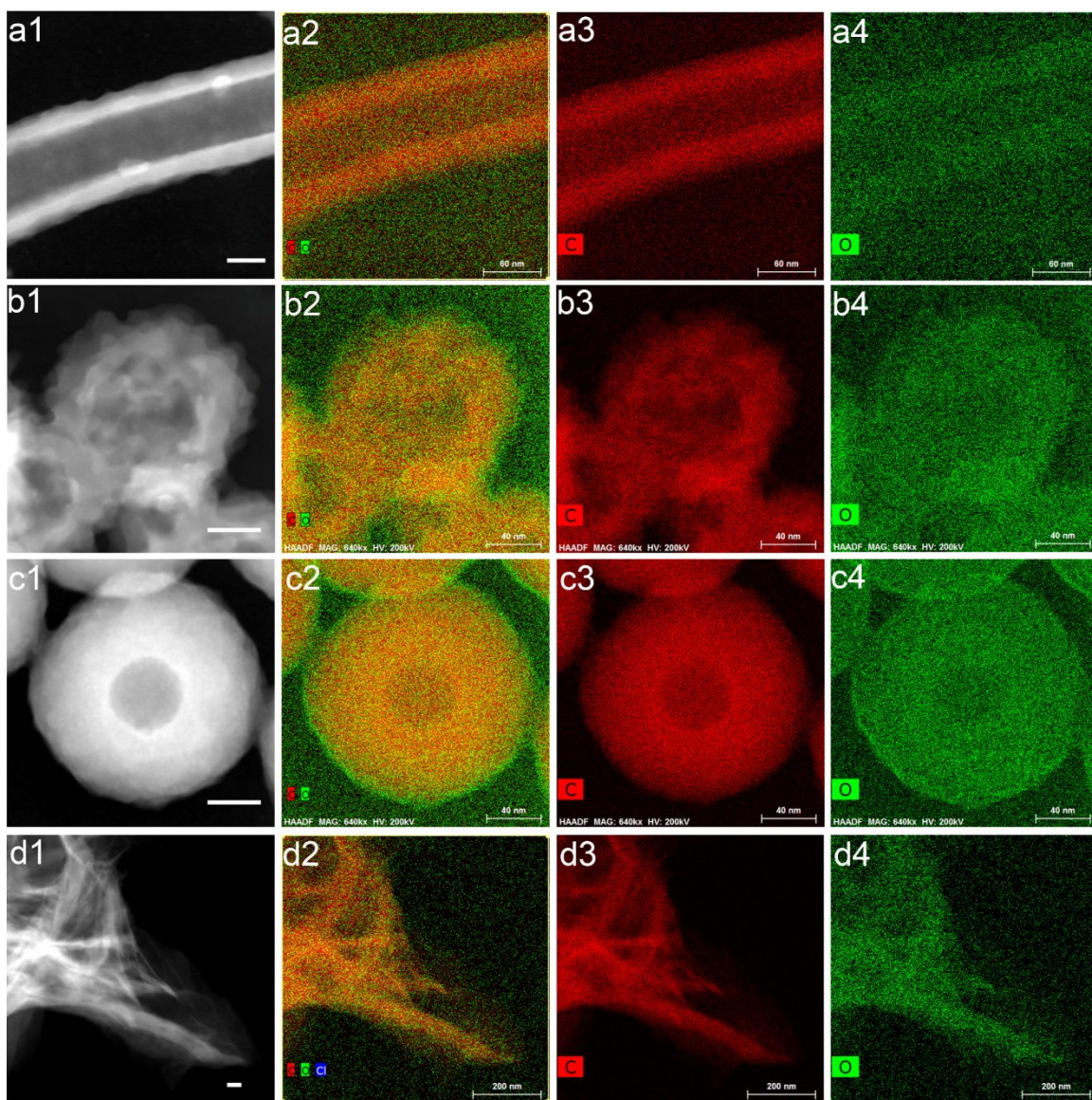
Figure S37. EDX-mapping images of the diverse morphology-controlled carbons. HAADF-STEM images of (a1) PNTs, (b1) PHNP-B, (c1) PHNP-N, and (d1) PNSs. EDX-mapping of (a2–4) PNTs, (b2–4) PHNP-B, (c2–4) PHNP-N, and (d2–4) PNSs. Scale bars: 40 nm.
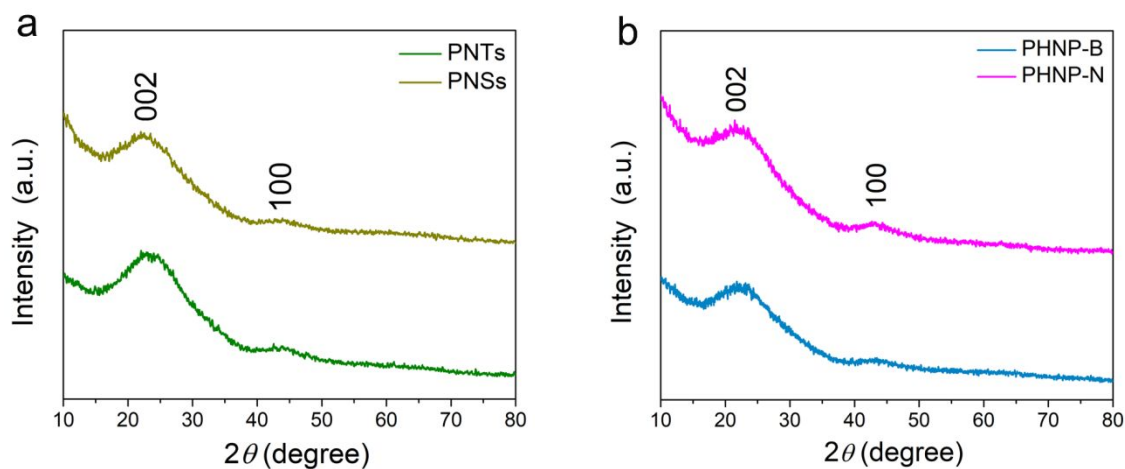
Figure S38. Powder XRD profiles for diverse morphology-controlled carbons.
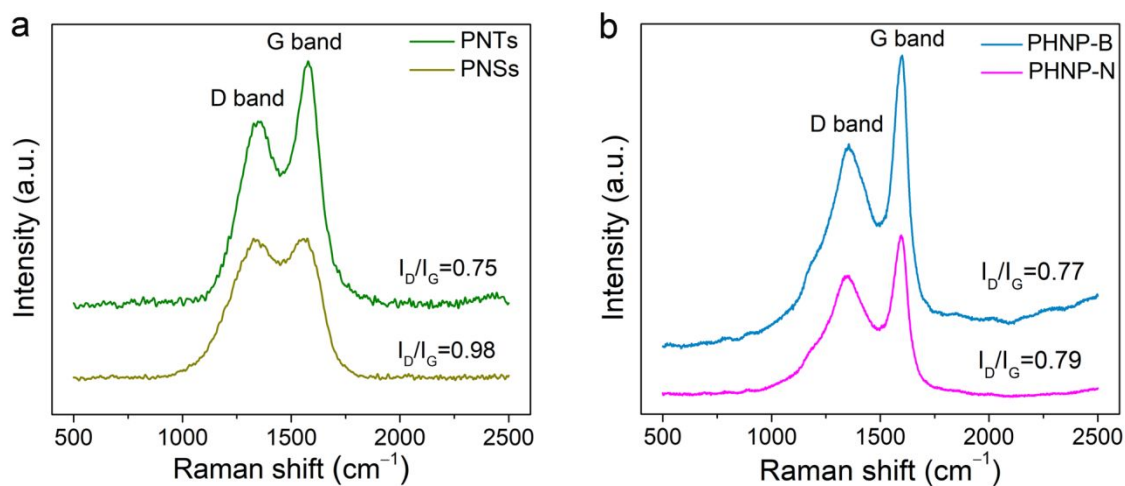
Figure S39. Raman spectra of the diverse morphology-controlled carbons. The spectra show a typical D-band at around 1359 cm^{-1} and a G-band at around 1590 cm^{-1}, indicating co-existence of amorphous and graphitic structures.
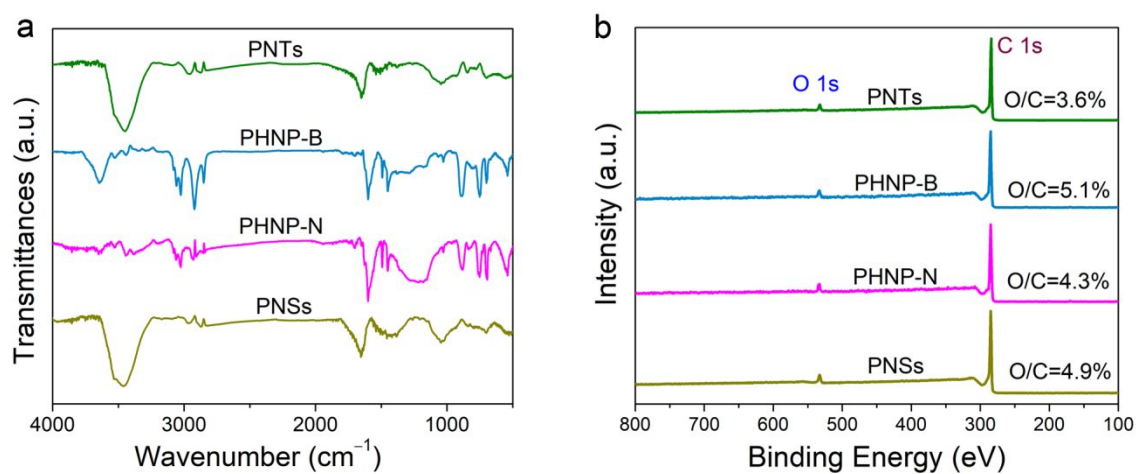
Figure S40. Characterizations of PHNPs. (a) The FT-IR spectra of the carbons, (b) XPS spectra of carbons.
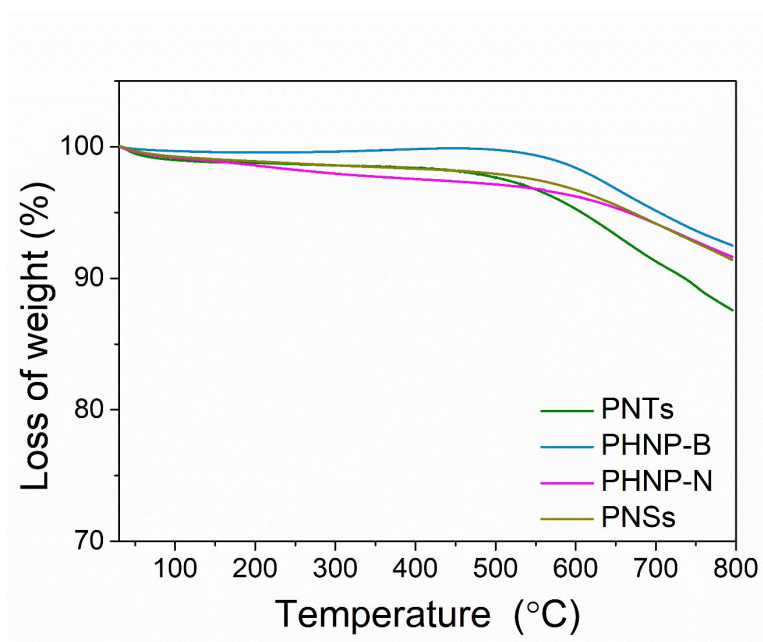
Figure S41. TGA spectra of the diverse morphology-controlled carbons.
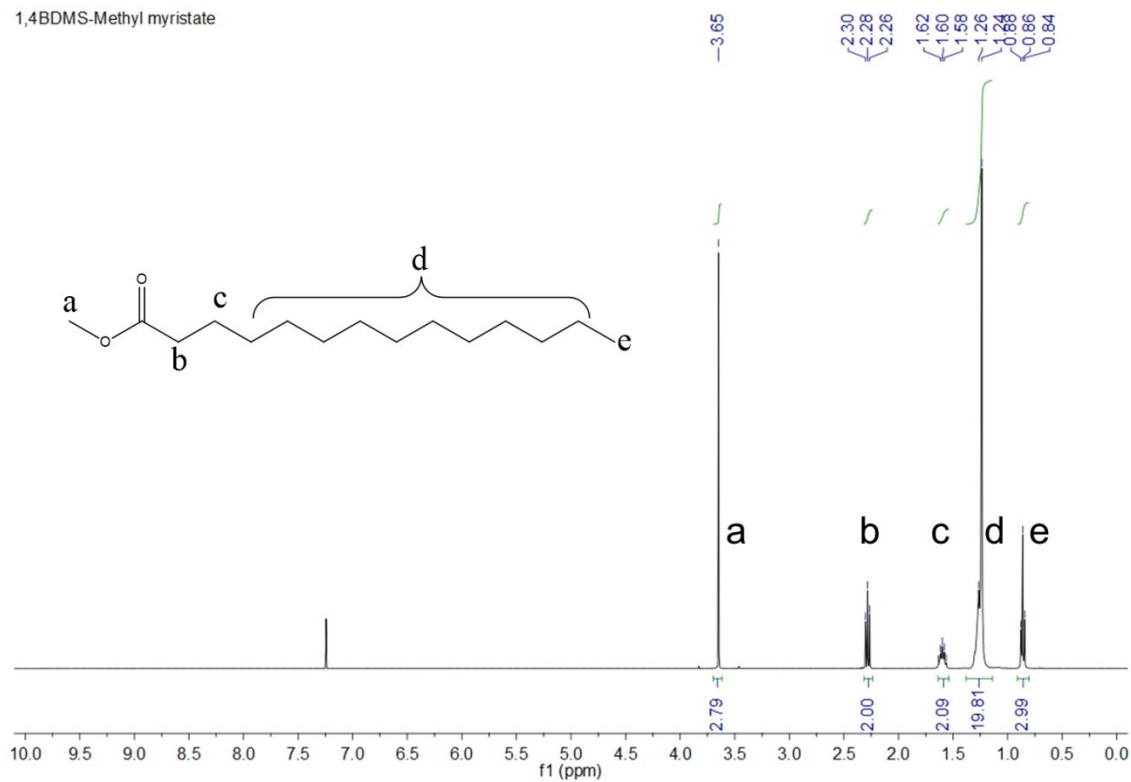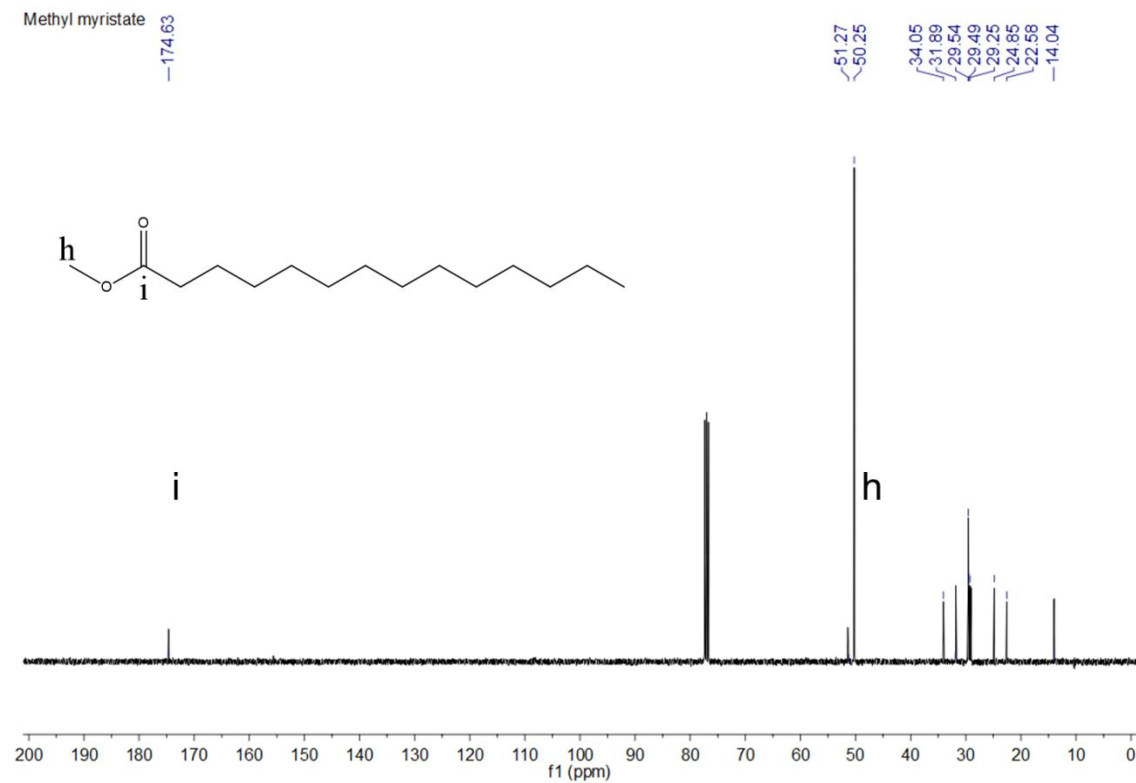
Figure S42. ^{1}H and ^{13}C NMR spectra of methyl myristate obtained by esterification using SHNP-B.

2,6NDMS-Methyl myristate

3.65

2.30 2.29 2.27

1.62 1.61 1.59 1.27 1.24

0.88 0.87 0.85

a   b   c d e

2.80   2.00   2.13 19.90 3.00

f1 (ppm)
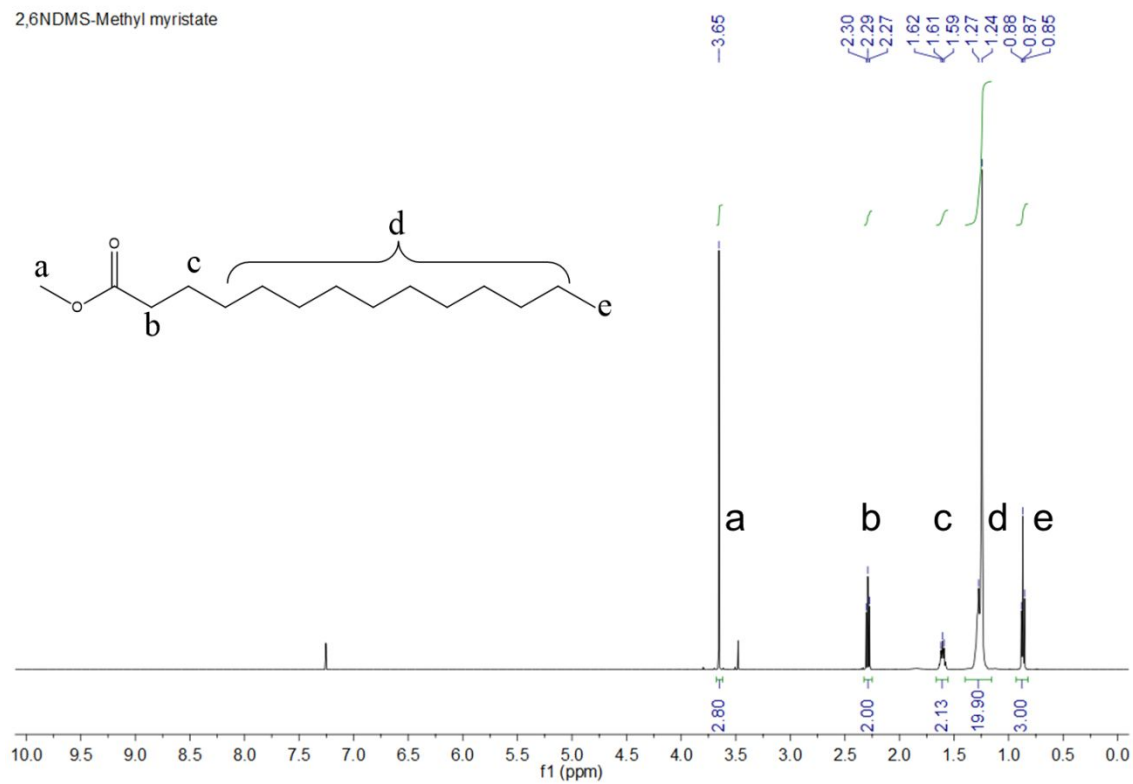
Figure S43. ^{1}H spectrum of methyl myristate obtained by esterification using SHNP-N.
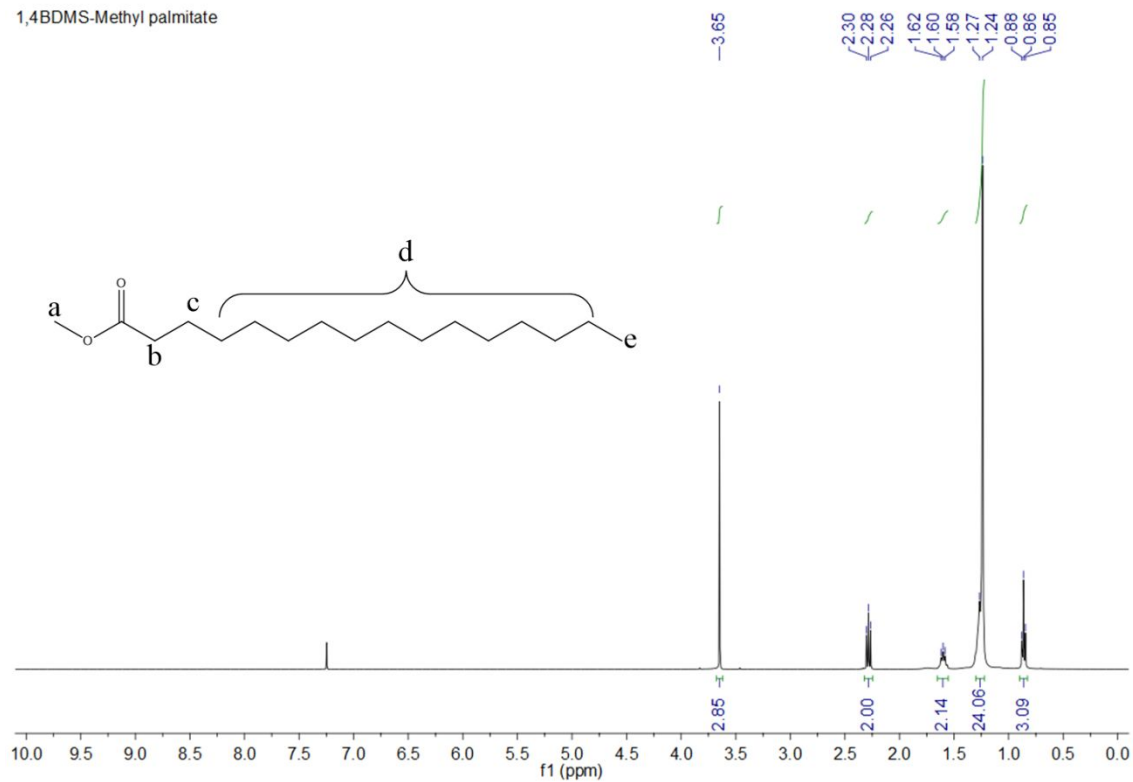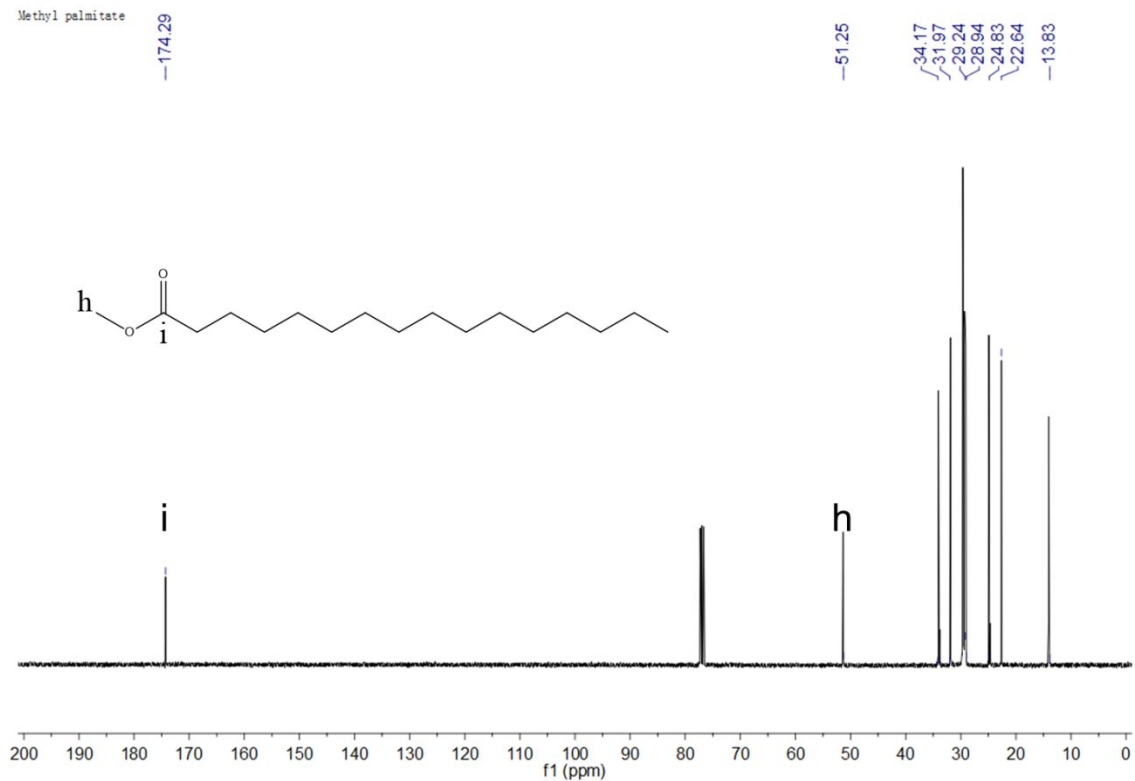
Figure S44. ^1H and ^{13}C NMR spectra of methyl palmitate obtained by esterification using SHNP-B.
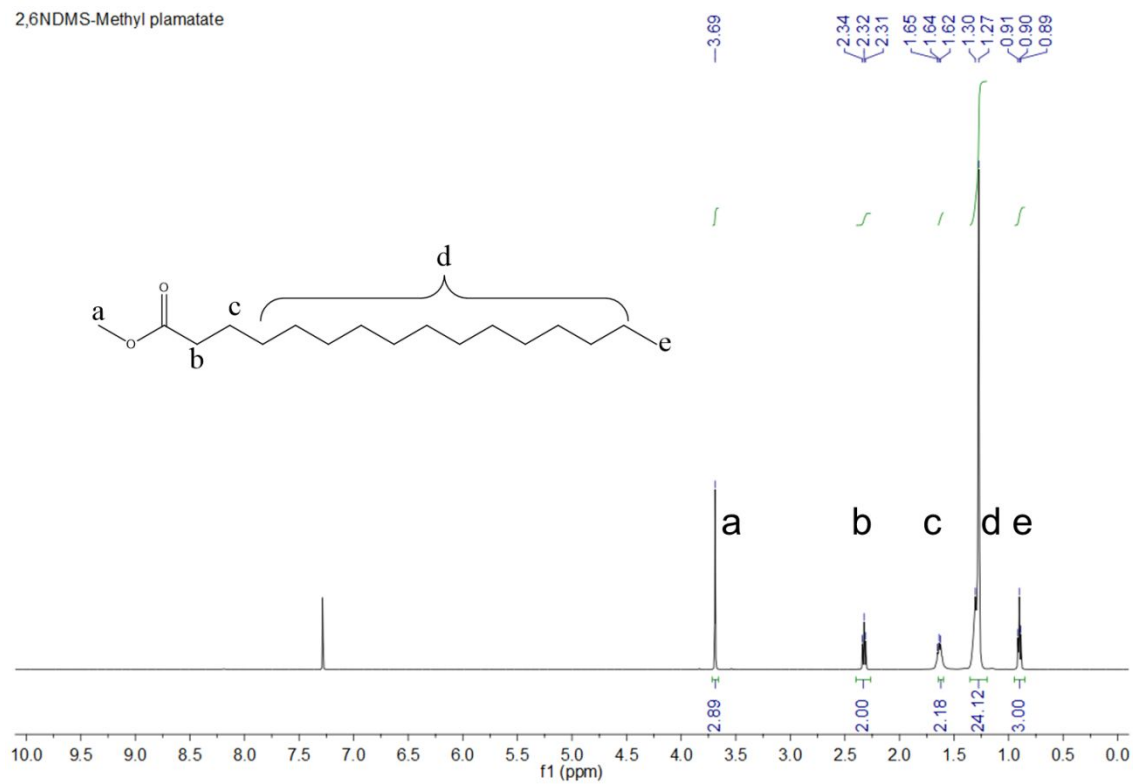
Figure S45. ^{1}H NMR spectrum of methyl palmitate obtained by esterification using SHNP-N.

1，4BDMS-Dimethyl glutarate
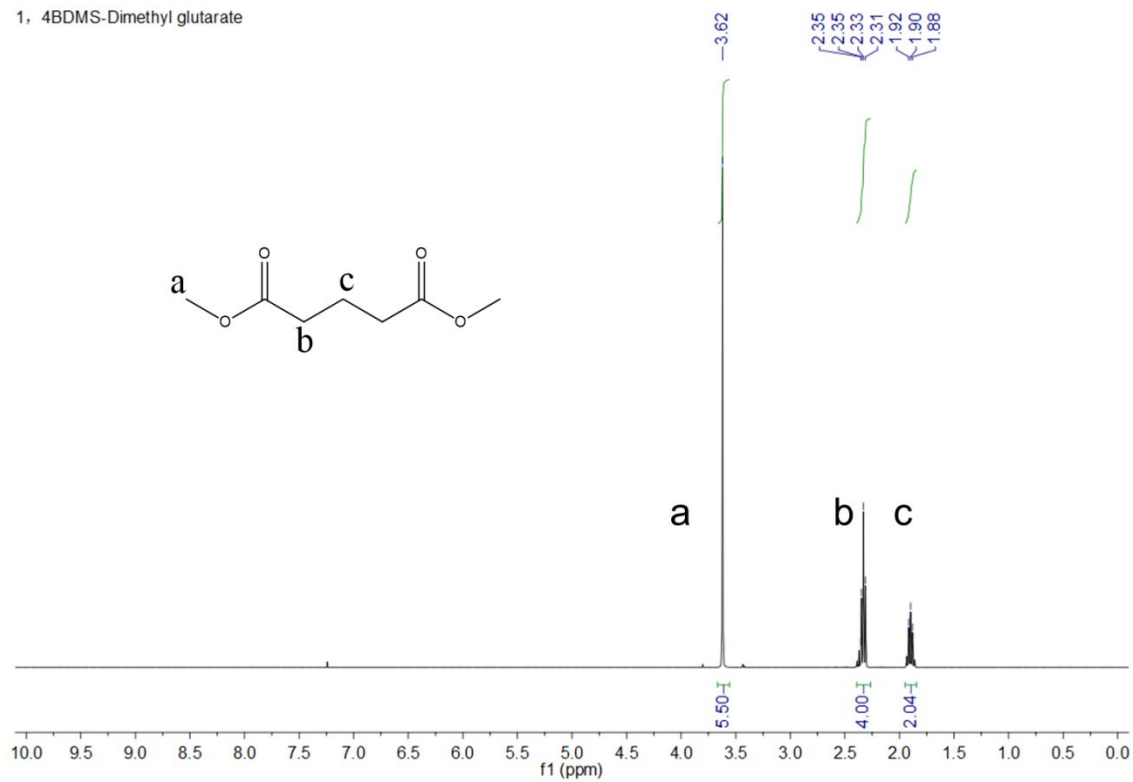
Dimethyl glutarate
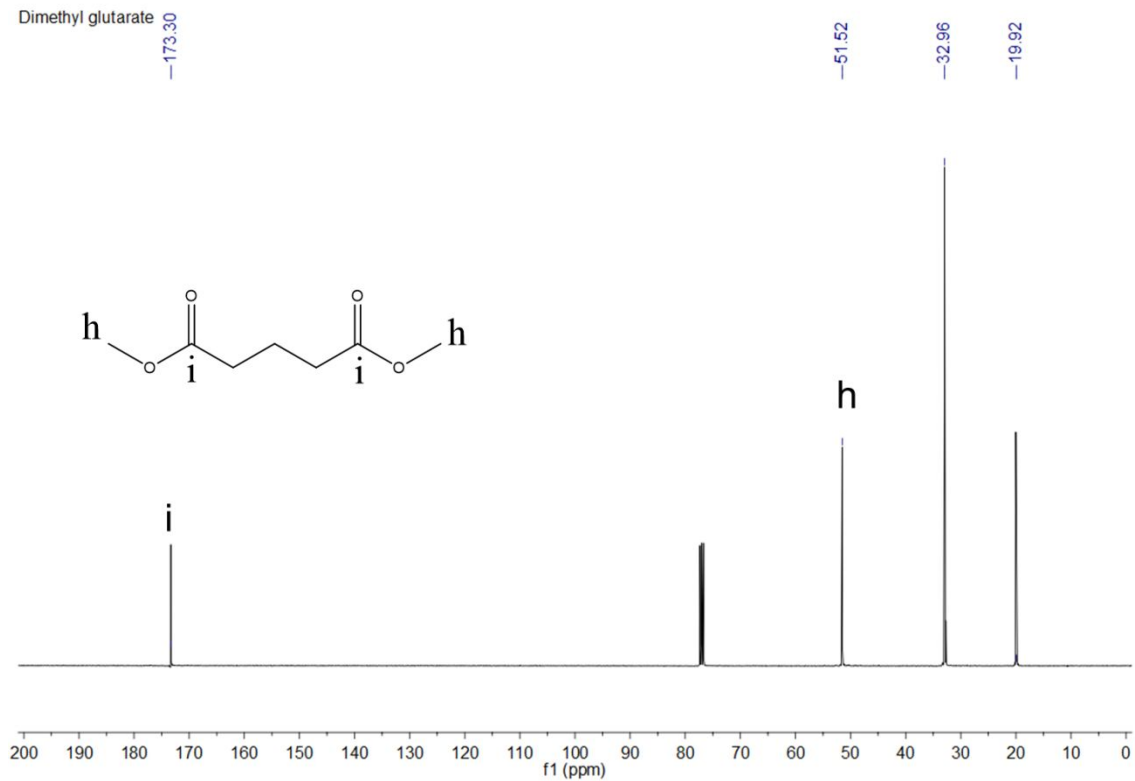
Figure S46. ^{1}H and ^{13}C NMR spectra of dimethyl glutarate obtained by esterification using SHNP-B.

2,6NDMS-Dimethyl glutarate

−3.68

2.40
2.39
2.37
1.97
1.96
1.96
1.94

a   b   c

5.34   4.00   2.01

10.0 9.5 9.0 8.5 8.0 7.5 7.0 6.5 6.0 5.5 5.0 4.5 4.0 3.5 3.0 2.5 2.0 1.5 1.0 0.5 0.0
f1 (ppm)
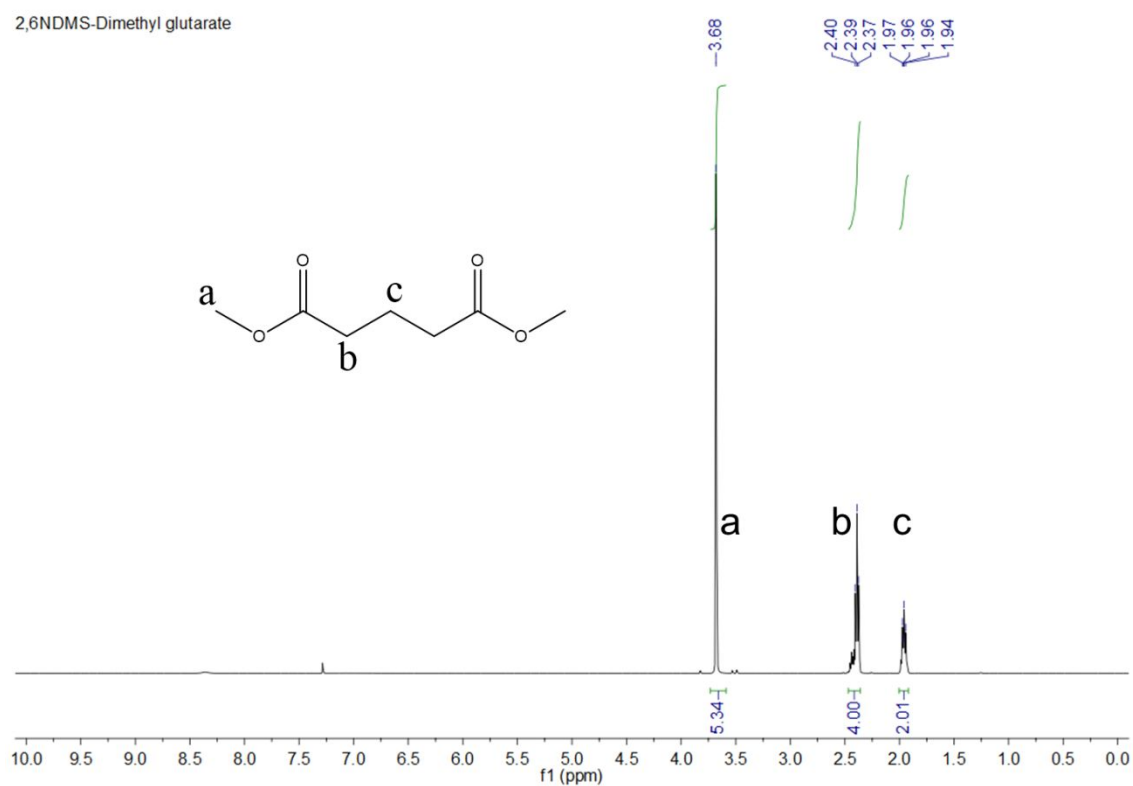
Figure S47. ^{1}H NMR spectrum of dimethyl glutarate obtained by esterification using SHNP-N.
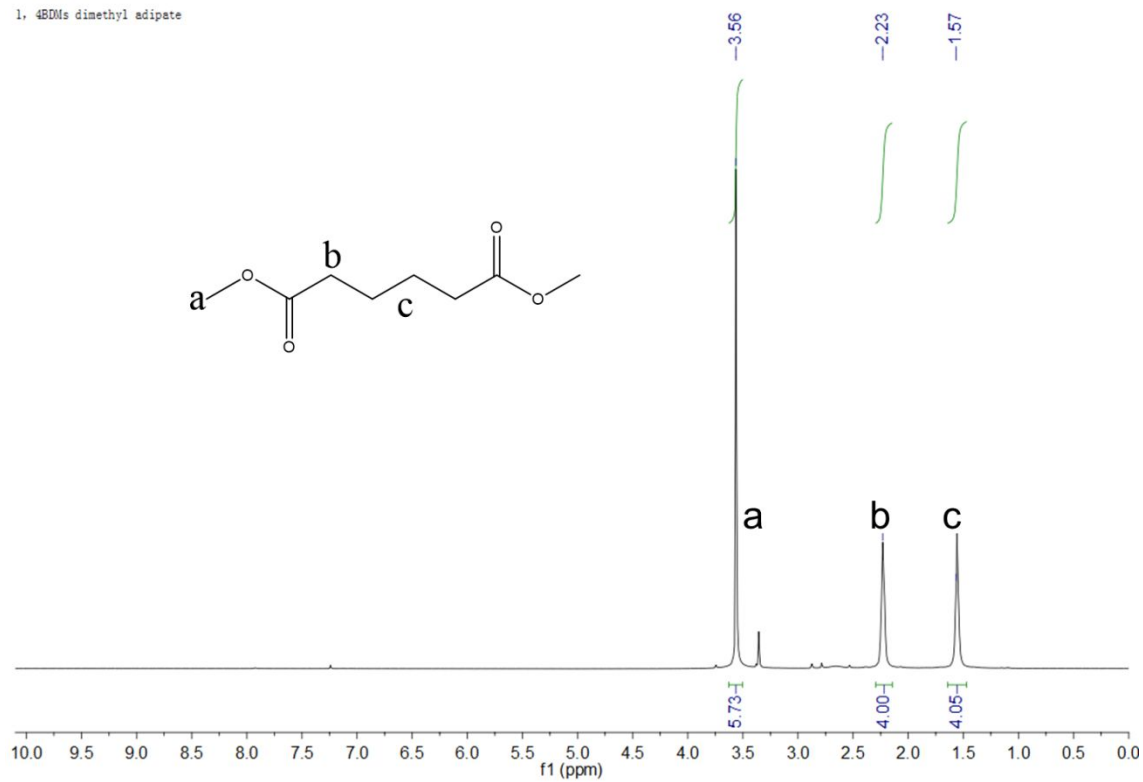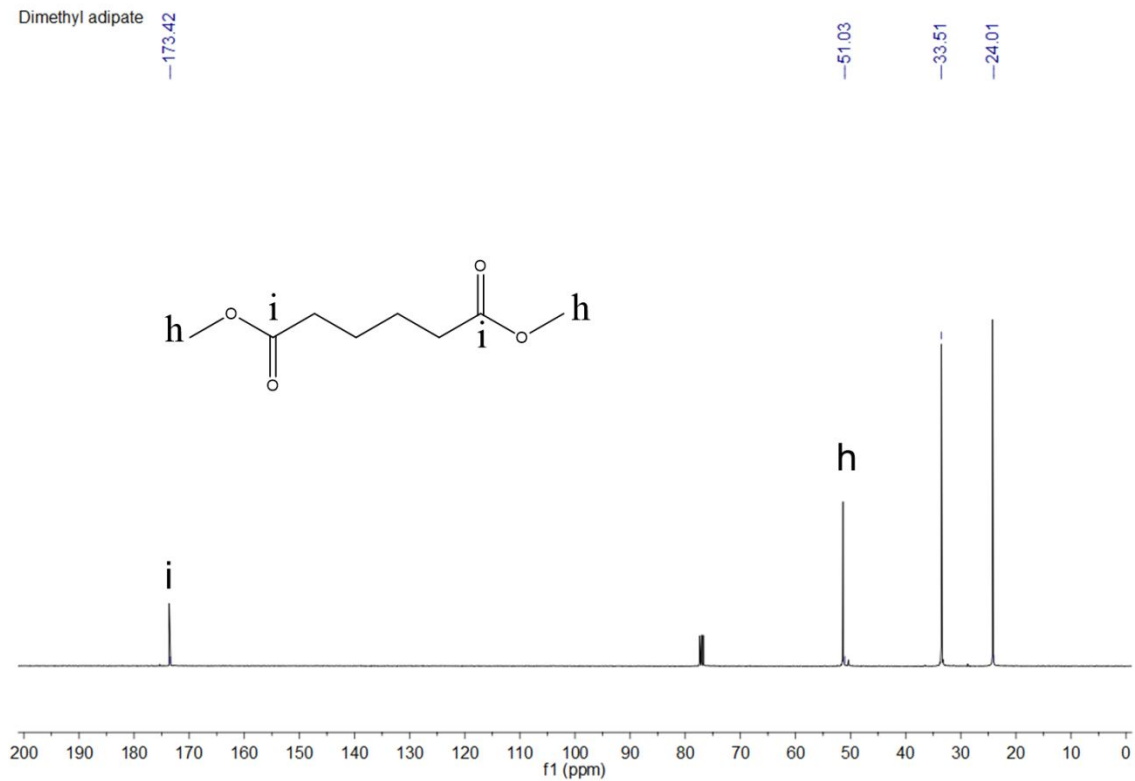
Figure S48. ¹H and ¹³ C NMR spectra of dimethyl adipate obtained by esterification using SHNP-B.
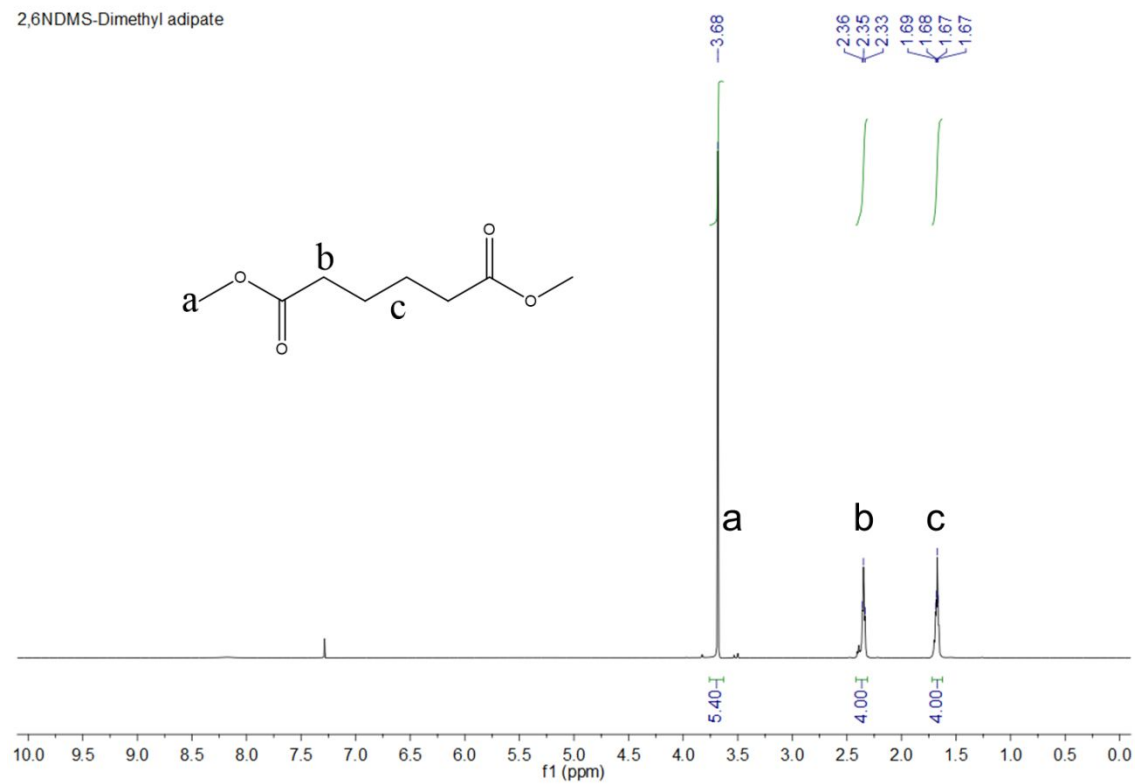
Figure S49. ^{1}H NMR spectrum of dimethyl adipate obtained by esterification using SHNP-N.

1,4BDMS-Soybean oil ester

—5.28
—3.60
—2.70
—2.23
—1.96
—1.55
—1.23
—1.23
—1.19
—1.18
—0.90
—0.89
—0.82
—0.81

0.04
1.00

10.0 9.5 9.0 8.5 8.0 7.5 7.0 6.5 6.0 5.5 5.0 4.5 4.0 3.5 3.0 2.5 2.0 1.5 1.0 0.5 0.0
f1 (ppm)

soybean oil ester

—174.38
—130.06
—127.65
—51.33
—33.87
—31.05
—29.11
—26.93
—24.76
—22.60
—20.63
—13.84

200 190 180 170 160 150 140 130 120 110 100 90 80 70 60 50 40 30 20 10 0
f1 (ppm)
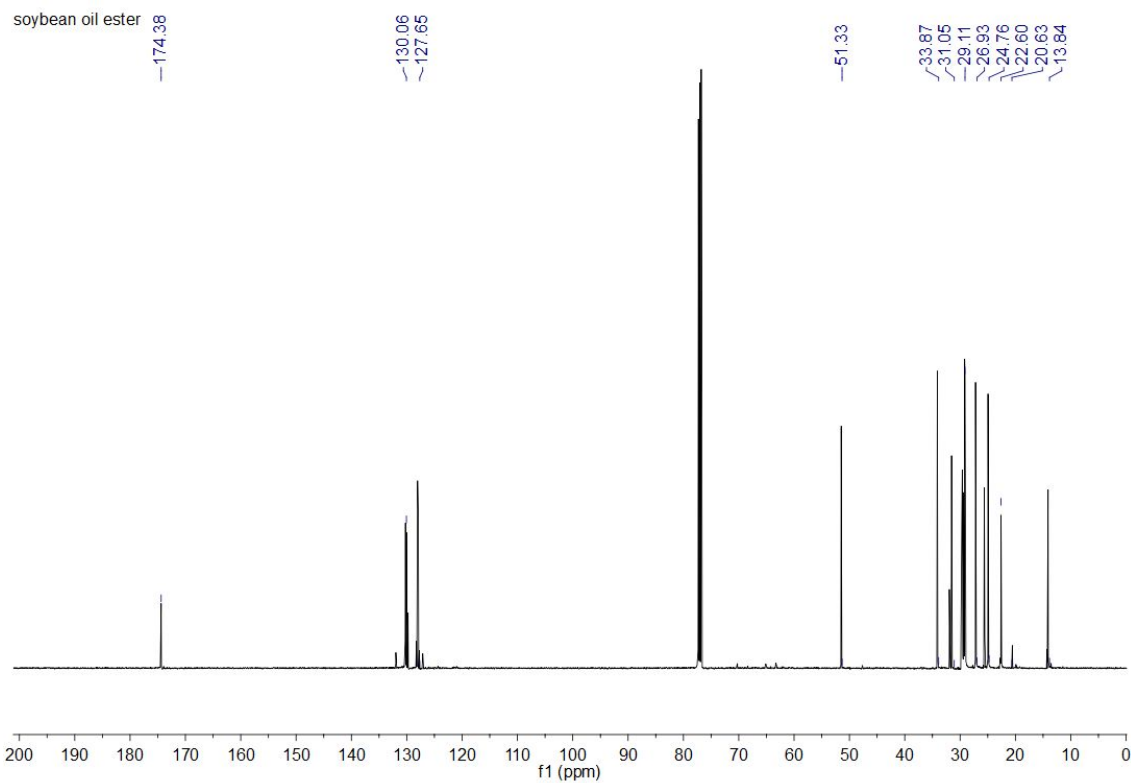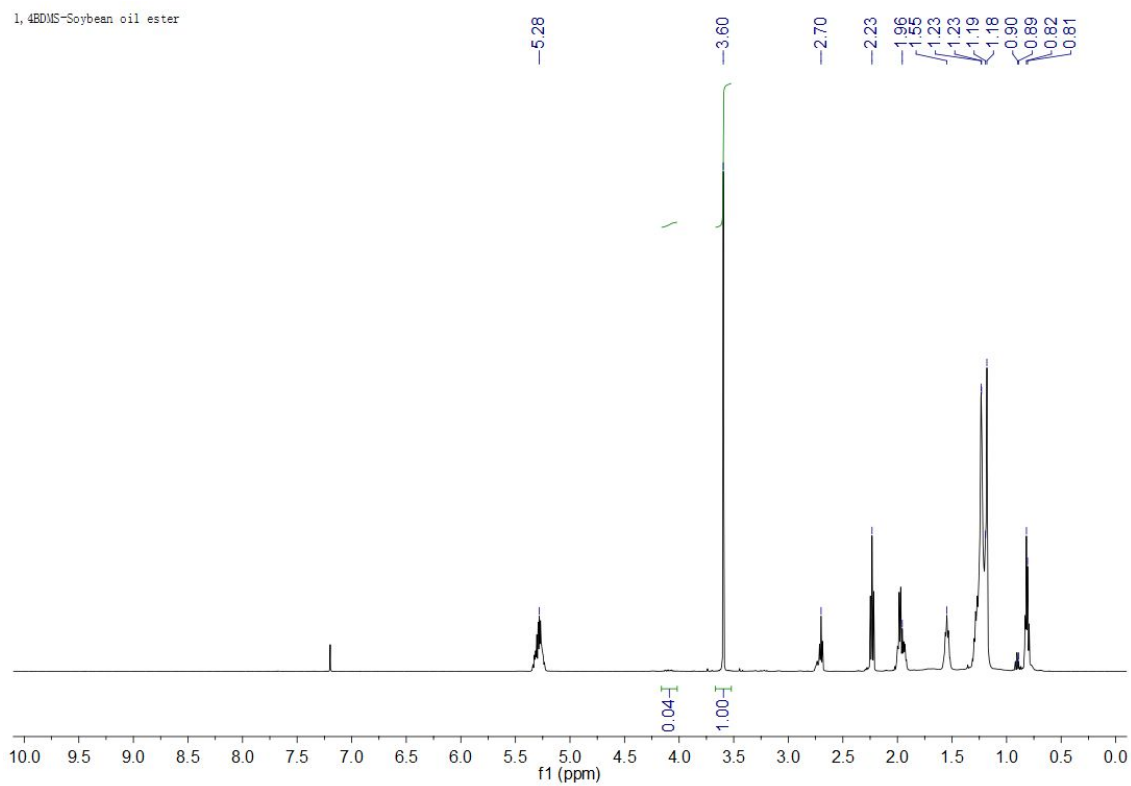
Figure S50. ^{1}H and ^{13}C NMR spectra of soybean oil ester obtained by transesterification using SHNP-B at optimized condition.

1,4BDMS-grape oil ester

−7.26

−5.33

−2.75
−2.28
−2.03
−1.61
−1.29
−0.87

0.02
1.00

grape oil ester

−174.13

130.22
128.35

−51.48

34.11
31.54
29.18
27.17
25.05
22.71
14.15
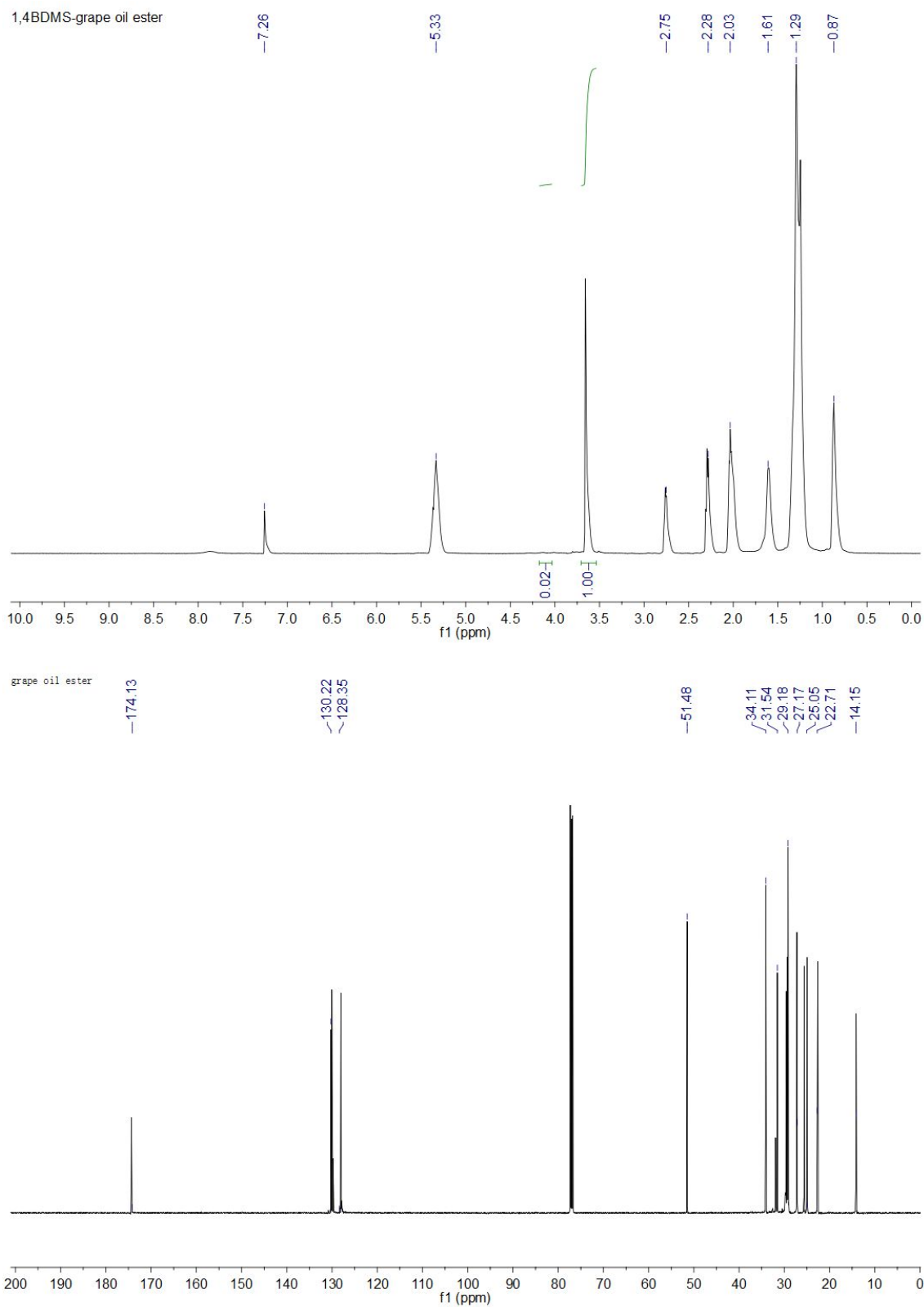
Figure S51. ^{1}H and ^{13}C NMR spectra of grape oil ester obtained by transesterification using SHNP-B at the optimized condition.

1, 4BDMS-olive oil ester

5.33

3.66

2.31
1.99
1.61
1.26
0.87

0.03
1.00

10.0 9.5 9.0 8.5 8.0 7.5 7.0 6.5 6.0 5.5 5.0 4.5 4.0 3.5 3.0 2.5 2.0 1.5 1.0 0.5 0.0
f1 (ppm)

olive oil ester

174.59

130.01
128.04

51.54

34.28
31.46
29.23
27.05
24.96
22.47
13.94

200 190 180 170 160 150 140 130 120 110 100 90 80 70 60 50 40 30 20 10 0
f1 (ppm)
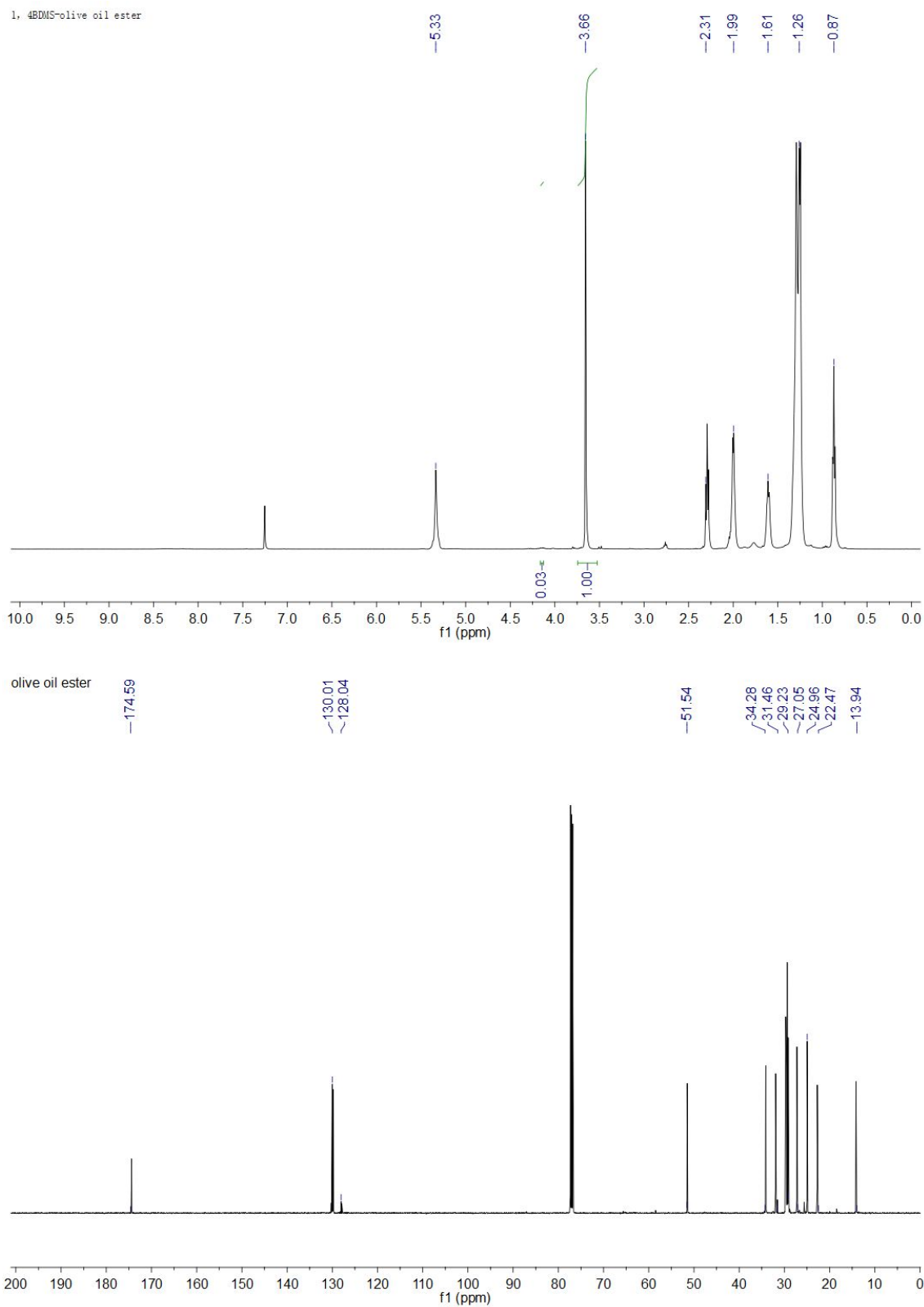
Figure S52. ^{1}H and ^{13}C NMR spectra of olive oil ester obtained by transesterification using SHNP-B at optimized condition.

1,4BDMS-canola oil ester

5.33

3.65

2.74
2.27
1.99
1.59
1.29
0.96
0.86

0.02
1.00

10.0 9.5 9.0 8.5 8.0 7.5 7.0 6.5 6.0 5.5 5.0 4.5 4.0 3.5 3.0 2.5 2.0 1.5 1.0 0.5 0.0
f1 (ppm)

canola oil ester

174.38

130.01
128.04

51.49

34.03
31.64
29.18
27.23
24.88
22.89

13.92

200 190 180 170 160 150 140 130 120 110 100 90 80 70 60 50 40 30 20 10 0
f1 (ppm)
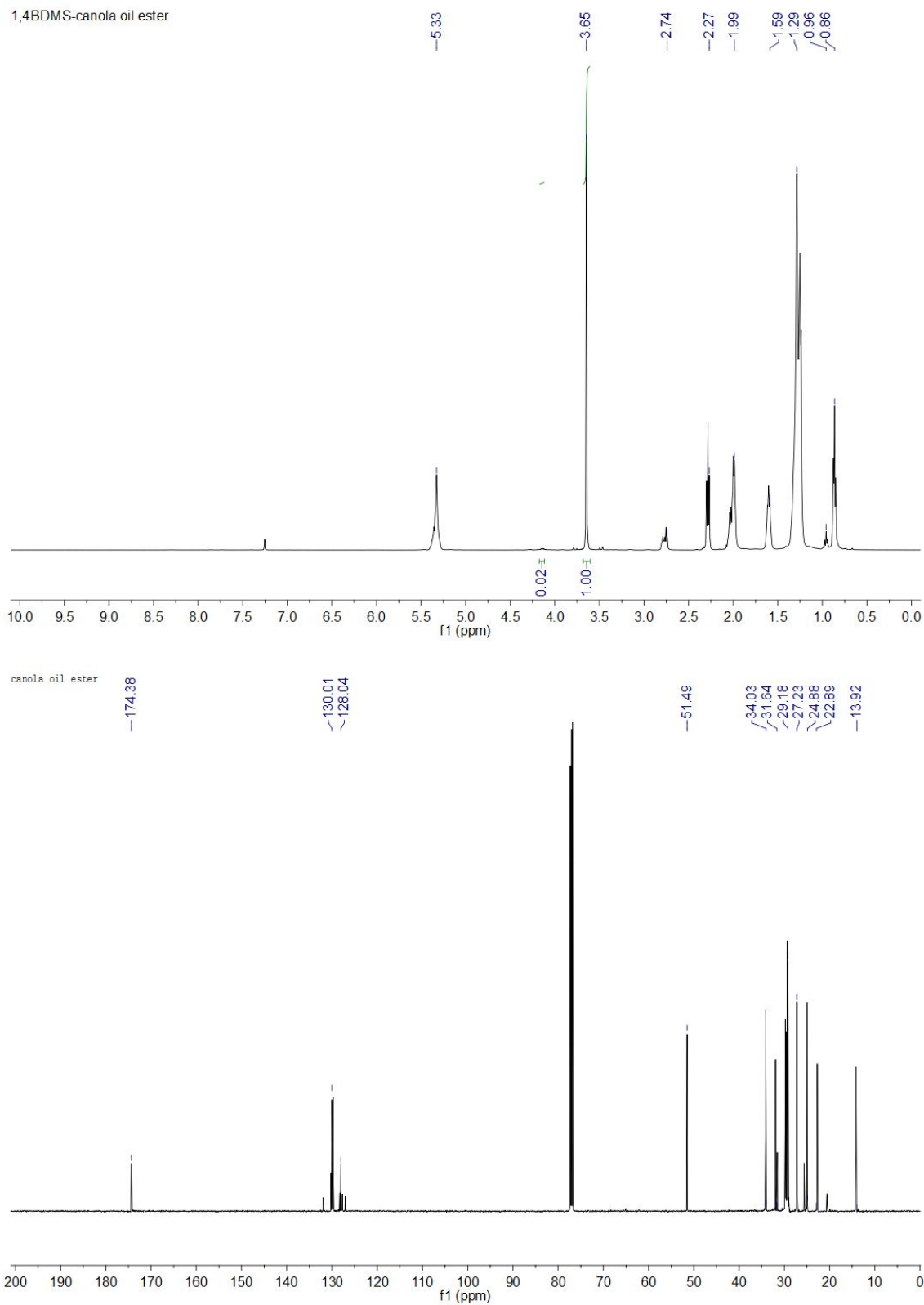
Figure S53. ^{1}H and ^{13}C NMR spectra of canola oil ester obtained by transesterification using SHNP-B at optimized conditions.

Analysis of the Figure 9e-g in the main text

The three-dimensional and two-dimensional contour maps (Figure 9e-g) in detail analysis: The Figure 9e clearly demonstrates that the soybean oil methyl esters (SMEs) yield enhances as the increase of reaction time, and this graph also shows that the SMEs yield increases with the growth of methanol to oil weight ratio because the excess solvent can improve the collision probabilities of reactant and catalyst molecules, shifting the equilibrium to the direction of the product. However, the continue increasing of mass ratio will not have a more significant effect on the yield by the reason of diluting the active sites of the catalyst (Figure 9e). The effect of interactions between methanol to oil weight ratio and reaction temperature are illustrated (Figure 9f), the SMEs yield gradually increase to the peak value at relative higher temperature and then slightly decrease when the temperature continues to increase. As one hand, higher temperature will helpful for the host-guest interaction for the molecules and then prompt the reaction course, on the other hand, too higher temperature will be accelerating methanol consumption, and lead to the decrease of SMEs yield. At last, we studied the effect of the temperature and reaction time on the SMEs (Figure 9g) yield. It could be found that the conversion rate of the SMEs yield increases as the reaction time and temperature increase, however, when achieve an identify conditions, the rate will apparent decline. (The Figure 9 in the main text)

Tables

Table S1. Representative examples of the synthetic protocols of morphology-controlled hyper cross-linked nanoporous polymers.

Monomer	Template	Cross-linker	Morphology	BET * surfaces area (m^2/g)	Ref.
Benzyl alcohol/ 1,4-Benzenedimethanol/ 2,6-Naphthalenemethanol/ 1,4-Bischloromethylbenzene	*F*	*F*	Nanotubes/ Hollow nanospheres/ Nanosheets	757/ 1142/ 1025	This work
Styrene and divinylbenzene	Hard template SiO_2	CME	Hollow nanospheres	626	S1
Poly(ethylene oxide)-*b*-polystyrene	Soft template	FDA	Hollow nanospheres /Mesoporous bulks	1123/ 439	S2
Benzene, biphenyl, 1,3,5-triphenylbenzene	*F*	*F*	Layers	1808	S3
Poly(methyl methacrylate)-*b*-polystyrene	Soft template	*F*	Hollow nanospheres	419	S4
Naphthalene, pyrene phenanthrene, anthracene	*F*	CME	Solid microspheres	456	S5
Benzene, anthracene, phenanthrene, pyrene	*F*	FDA	Nanotubes	1034	S6
Polylactide-*b*-polystyrene	Soft template	CCl_4	Hollow nanospheres	806	S7
Triphenylamine, and a,a'-dibromo-p-xylene	*F*	DPX	Nanosheets	1269	S8
Poly(glycidyl methacrylate)-*g*-(poly(lactide)-*b*-polystyrene/poly(4-vinylbenzyl chloride))	Soft template	FDA	Nanotubes	940	S9
Styrene-co-divinylbenzene, styrene	Fiber by electrospinning/ Polystyrene sphere	FDA	Nanofibers/ Nanosphere arrays	820/ 507	S10

FDA: Formaldehyde dimethyl acetal   CME: Chloromethyl methyl ether   DPX: α,α′-dibromo-p-xylene
F: Free   * The highest BET surface area reported in the article

Table S2. Summary of the elemental content for HCPs, SHNPs, and carbons.

Polymer	Element content (At. %)			
	C	O	Cl	S
HNTs	96.78	3.22		
HHNP-B	91.96	8.04		
HHNP-N	92.04	7.96		
HNSs	90.87	5.26	3.85	
SHNP-B	70.2	23.67		6.14
SHNP-N	66.42	26.61		6.97
PNTs	96.50	3.49		
PHNP-B	95.14	4.86		
PHNP-N	95.92	4.08		
PNSs	95.28	4.67	0.05	

The data is from the XPS.

Table S3. Summary of the elemental content for HCPs and SHCPs, and the cross-linking degrees.

Polymer	Element content (Wt. %)					Cross-linking degree (%)
	C	H	O	Cl	S	
HNTs	87.3	4.7	3.51			76.3
HHNP-B	79.25	4.71	6.91			70.2
HHNP-N	78.13	4.64	7.85			53.8
HNSs	81.62	5.10	5.3	5.02		87.6
SNTs	56.78	4.95	23.50		6.03	
SHNP-B	40.03	5.09	38.55		10.33	
SHNP-N	47.5	4.68	39.93		10.75	
SNSs	60.08	4.46	29.02		7.70	

The data is from the elemental analysis. Crosslinking degree = $(O_{Monomer}-O_{Polymer})$ *100%/ $O_{Monomer}$, specially, the crosslinking degree of HNSs is calculated by the chlorine content.

Table S4. Summary of the pore structure parameters of samples.

Polymer	S_{BET}^{a} (m^2/g)	V_{tot}^{b} (cc/g)	D_p^{c} (nm)
HNTs	757	0.97	5.11
HHNP-B	1069	1.45	6.23
HHNP-N	1142	1.32	4.61
HNSs	1025	0.99	3.84
SA-HHNP-B	956	0.68	2.82
HCPP-B	1098	0.943	3.23
HCPP-N	1016	0.763	2.99
SHNP-B	506	0.86	6.34
SHNP-N	524	0.67	3.94

[a] BET surface area from N$_2$ adsorption. [b] total pore volume (P/P$_0$=0.99). [c] the average pore size diameter.

Table S5. Effect of monomer concentration on morphology of the hyper-cross-linked porous polymer (HCP).

Conc.* \ Polymer	5	7.5	10	20	50	100	200	500	1000
HCP-BA	particle	fiber particle	fiber sphere	sphere	HNT	HNT	tube-paticle	particle	–
HCP-B	nano worm	HHNP	HHNP	HHNP	sphere-tube	sphere-tube	particle	particle	particle
HCP-N	small sphere	HHNP	HHNP	solid-sphere	particle	particle	particle	particle	–
HCP-BCB	flower-like	HNS	HNS	HNS	flake	flake	bulk	bulk	–
SA-HCP -B	–	–	HHNP	solid sphere	–	–	–	–	–

The experiments were carried on the same conditions, the polymers achieved by the 1,4benzenedimethanol/FeCl$_3$, 2,6naphthalenedimethanol/FeCl$_3$, 1,4 bis-chloromethyl benzene/FeCl$_3$, benzyl alcohol/FeCl$_3$, 1,4benzenedimethanol/concentrated sulfuric acid were

named as HCP-B, HCP-N, HCP-BCB, HCP-BA, SA-HCP-B, respectively. *: monomer concentration (mmol/L).

Table S6. Esterification reactions of diverse fatty acids over SHNP-B and SHNP-N.

Entry	Fatty acid	Catalyst	Temperature (℃)	Yield (%)
1	Myristic acid	HHNP-B	25	3.1
2	Myristic acid	SHCP-B	25	65.5
3	Myristic acid	SHNP-B	25	93
4	Myristic acid	SHNP-N	25	93.5
5	Palmitic acid	SHNP-B	25	95
6	Palmitic acid	SHNP-N	25	96.4
7	Glutaric acid	SHNP-B	25	91.6
8	Glutaric acid	SHNP-N	25	89.1
9	Adipic acid	SHNP-B	25	95.6
10	Adipic acid	SHNP-N	25	90.1

Table S7. Experimental results and predicted responses for the transesterification of soybean oil.

Run	Code factors			SME-SHNP-B (%)		
	X_1	X_2	X_3	Experimental Actual value	Predicted	Relative dev. (%)
1	0.000	0.000	0.000	80.1	79.08	1.27
2	0.000	0.000	0.000	77.5	79.08	−2.04
3	0.000	0.000	0.000	79.6	79.08	0.65
4	1.000	−1.000	0.000	70.1	70.25	−0.21
5	0.000	0.000	0.000	79.8	79.08	0.90
6	1.000	1.000	0.000	80.7	80.42	0.35
7	0.000	1.000	1.000	86.3	87.34	−1.21
8	0.000	−1.000	1.000	70.1	70.71	−0.87
9	−1.000	0.000	1.000	82.8	81.91	1.07
10	−1.000	0.000	−1.000	13.4	14.16	−5.70
11	1.000	0.000	1.000	90.1	89.34	0.84
12	0.000	−1.000	−1.000	10.2	9.16	10.2
13	0.000	0.000	0.000	78.4	79.08	−0.87
14	0.000	1.000	−1.000	16.2	15.59	3.77
15	1.000	0.000	−1.000	22.9	23.79	−3.89
16	−1.000	−1.000	0.000	60.1	60.37	−0.45
17	−1.000	1.000	0.000	73.4	73.25	0.20

Relative deviation (%) = (actual − predicted)100/actual.

Table S8. The standard analysis of variance (ANOVA) for the fitted polynomial quadratic model.

Source	SHNP-B				
	Sum of squares	Df	Mean square	F-value	p-value prob $> F$
model	12533.24	9	1392.58	917.42	< 0.0001
X_1	145.35	1	145.35	95.76	< 0.0001
X_2	265.65	1	265.65	175.01	< 0.0001
X_3	8884.44	1	8884.44	5853.01	< 0.0001
X_1X_2	1.82	1	1.82	1.20	0.3095
X_1X_3	1.21	1	1.21	0.7971	0.4016
X_2X_3	26.01	1	26.01	17.14	0.0044
X_{12}	2.08	1	2.08	1.37	0.2803
X_{22}	224.53	1	224.53	147.92	< 0.0001
X_{32}	2863.31	1	2863.31	1886.33	< 0.0001
Residual	10.63	7	1.52		
Lack of fit	5.84	3	1.95	1.63	0.3176
Pure error	4.79	4	1.20		

Std.dev,	R^2	Adj R^2	Pre R^2	Mean	Adeq precision
1.23	0.9992	0.9981	0.9920	63.04	84.8472
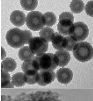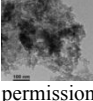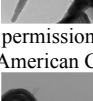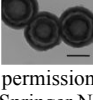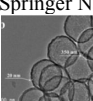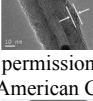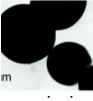
The Model F-value of 917.42 implies the model is significant. There is only a 0.01% chance that an F-value this large could occur due to noise, the p-values less than 0.0500 indicate model terms are significant. In this case A, B, C, BC, B², C² are significant model terms.

Table S9. Transesterification Reactions of various oils over SHNP-B and SHNP-N.

Entry	Oil	Catalyst	Temperature (℃)	Yield (%)
1	Soybean oil	SHNP-B	70	91.1
2	Soybean oil	SHNP-N	70	93.68
3	Grape oil	SHNP-B	70	95.69
4	Grape oil	SHNP-N	70	94.07
5	Olive oil	SHNP-B	70	94.6
6	Olive oil	SHNP-N	70	91.7
7	Canola oil	SHNP-B	70	94.8
8	Canola oil	SHNP-N	70	89.8

Table S10. Comparison of various porous solid acid catalysts used for the esterification of fatty acids (FFA). Myristic acid (MA), oleic acid (OA), lauric acid (LA).

Catalyst (amount)	Morphology	FFA (amount)	Time (h)	Temp. (℃)	Yield (%)	Ref.
SHNP-B (10 mg)		MA (1 mmol)	6	25	93	This work
SHNP-N (10 mg)		MA (1 mmol)	6	25	93.5	This Work
HMP-1-SO$_3$H (10 mg)	Adapted with permission from ref S11. Copyright 2015 Royal Society of Chemistry.	MA (0.5 mmol)	10	25	99	S11
SPPOP-3 (17 mg)	Adapted with permission from ref S12. Copyright 2015 American Chemical Society.	LA (1 mmol)	10	25	94	S12
PS-SO$_3$H @mesosilicas DSNs (50 mg)	Adapted with permission from ref S13. Copyright 2014 Springer Nature Publishing.	LA (2 mmol)	6	80	89.7	S13
HS/C-SO$_3$H (100 mg)	Adapted with permission from ref S14. Copyright 2015 American Chemical Society.	OA (10 mmol)	5	80	98.8	S14
CNT-P-SO$_3$H (20 mg)	Adapted with permission from ref S15. Copyright 2016 American Chemical Society.	OA (1 mmol)	10	60	93	S15
OPPSO$_3$H-1 (10 mg)	Adapted with permission from ref S16. Copyright 2018 Royal Society of Chemistry.	MA (1 mmol)	5	70	97	S16
Sg-CN (25 mg)	Adapted with permission from ref S17 under a Creative Commons License.	OA (1.0 g)	4	25	99	S17
HMONs-SO$_3$H (5 mg)	Adapted with permission from ref S18. Copyright 2018 Elsevier.	LA (0.5 mmol)	2.5	65	99	S18

References

(S1) Jia, Z.; Wang, K.; Tan, B.; Gu, Y. Hollow Hyper-Cross-Linked Nanospheres with Acid and Base Sites as Efficient and Water-Stable Catalysts for One-Pot Tandem Reactions. *ACS Catal.* **2017**, *7*, 3693–3702.

(S2) Gao, T. N.; Wang, T.; Wu, W.; Liu, Y.; Huo, Q.; Qiao, Z. A.; Dai, S. Solvent-Induced Self-Assembly Strategy to Synthesize Well-Defined Hierarchically Porous Polymers. *Adv. Mater.* **2019**, *31*, 1806254.

(S3) Wang, S.; Zhang, C.; Shu, Y.; Jiang, S.; Xia, Q.; Chen, L.; Jin, S.; Hussain, I.; Cooper, A. I.; Tan, B. Layered Microporous Polymers by Solvent Knitting Method. *Sci. Adv.* **2017**, *3*, e1602610.

(S4) Li, Z.; Wu, D.; Huang, X.; Ma, J.; Liu, H.; Liang, Y.; Fu, R.; Matyjaszewski, K. Fabrication of Novel Polymeric and Carbonaceous Nanoscale Networks by the Union of Self-Assembly and Hypercrosslinking. *Energy Environ. Sci.* **2014**, *7*, 3006–3012.

(S5) Huang, X.; Kim, S.; Heo, M. S.; Kim, J. E.; Suh, H.; Kim, I. Easy Synthesis of Hierarchical Carbon Spheres with Superior Capacitive Performance in Supercapacitors. *Langmuir* **2013**, *29*, 12266–12274.

(S6) Wang, X.; Mu, P.; Zhang, C.; Chen, Y.; Zeng, J.; Wang, F.; Jiang, J.-X. Control Synthesis of Tubular Hyper-Cross-Linked Polymers for Highly Porous Carbon Nanotubes. *ACS Appl. Mater. Interfaces* **2017**, *9*, 20779–20786.

(S7) He, Z.; Zhou, M.; Wang, T.; Xu, Y.; Yu, W.; Shi, B.; Huang, K. Hyper-Cross-Linking Mediated Self-Assembly Strategy to Synthesize Hollow Microporous Organic Nanospheres. *ACS Appl. Mater. Interfaces* **2017**, *9*, 35209–35217.

(S8) Mondal, S.; Patra, B. C.; Bhaumik, A. One-Pot Synthesis of Polyhydroquinoline Derivatives through Organic-Solid-Acid-Catalyzed Hantzsch Condensation Reaction. *ChemCatChem* **2017**, *9*, 1469–1475.

(S9) Yu, W.; Zhou, M.; Wang, T.; He, Z.; Shi, B.; Xu, Y.; Huang, K. "Click Chemistry" Mediated Functional Microporous Organic Nanotube Networks for Heterogeneous Catalysis. *Org. Lett.* **2017**, *19*, 5776–5779.

(S10) Liu, H.; Li, S.; Yang, H.; Liu, S.; Chen, L.; Tang, Z.; Fu, R.; Wu, D. Stepwise Crosslinking: A Facile yet Versatile Conceptual Strategy to Nanomorphology-Persistent Porous Organic Polymers. *Adv. Mater.* **2017**, *29*, 1700723.

(S11) Bhunia, S.; Banerjee, B.; Bhaumik, A. A New Hypercrosslinked Supermicroporous Polymer, with Scope for Sulfonation, and Its Catalytic Potential for the Efficient Synthesis of Biodiesel at Room Temperature. *Chem. Commun.* **2015**, *51*, 5020–5023.

(S12) Kundu, S. K.; Bhaumik, A. Pyrene-Based Porous Organic Polymers as Efficient Catalytic Support for the Synthesis of Biodiesels at Room Temperature. *ACS Sustain. Chem. Eng.* **2015**, *3*, 1715–1723.

(S13) Zhang, X.; Zhao, Y.; Xu, S.; Yang, Y.; Liu, J.; Wei, Y.; Yang, Q. Polystyrene Sulphonic Acid Resins with Enhanced Acid Strength *via* Macromolecular Self-Assembly within Confined Nanospace. *Nat. Commun.* **2014**, *5*, 3170.

(S14) Wang, Y.; Wang, D.; Tan, M.; Jiang, B.; Zheng, J.; Tsubaki, N.; Wu, M. Monodispersed Hollow SO_3H-Functionalized Carbon/Silica as Efficient Solid Acid Catalyst for Esterification of Oleic Acid. *ACS Appl. Mater. Interfaces* **2015**, *7*, 26767–26775.

(S15) Liu, H.; Chen, J.; Chen, L.; Xu, Y.; Guo, X.; Fang, D. Carbon Nanotube-Based Solid Sulfonic Acids as Catalysts for Production of Fatty Acid Methyl Ester *via* Transesterification and Esterification. *ACS Sustain. Chem. Eng.* **2016**, *4*, 3140–3150.

(S16) Varyambath, A.; Kim, M.-R.; Kim, I. Sulfonic Acid-Functionalized Organic Knitted Porous Polyaromatic Microspheres as Heterogeneous Catalysts for Biodiesel Production. *New J. Chem.* **2018**, *42*, 12745–12753.

(S17) Baig, R. N.; Verma, S.; Nadagouda, M. N.; Varma, R. S. Room Temperature Synthesis of Biodiesel Using Sulfonated Graphitic Carbon Nitride. *Sci. Rep.* **2016**, *6*, 39387.

(S18) Wang, T.; Xu, Y.; He, Z.; Zhou, M.; Yu, W.; Shi, B.; Song, C.; Huang, K. Fabrication of Sulphonated Hollow Porous Nanospheres and Their Remarkably Improved Catalytic Performance for Biodiesel Synthesis. *React. Funct. Polym.* **2018**, *132*, 98–103.